Sea Surface Oil Slick Detection and Wind Field Measurement Using Global Navigation Satellite System Reflectometry

by

©Chen Li, B.Eng.

A thesis submitted to the School of Graduate Studies in partial fulfillment of the requirements for the degree of

Master of Engineering

Electrical Engineering, Faculty of Engineering and Applied Science

Memorial University of Newfoundland

May, 2014

St. John's Newfoundland

Abstract

In this thesis, research for improving sea surface remote sensing using the Global Navigation Satellite System-Reflectometry (GNSS-R) signals is presented. Firstly, a method to enable the simulation of GNSS-R delay Doppler Map (DDM) of an oil slicked sea surfaces under general scenarios is proposed. The DDM of oil slicked sea surface under general scenarios is generated by combining the mean-square slope model for oil slicked/clean surfaces and the GNSS-R Zavorotny-Voronovich (Z-V) scattering model. The coordinate system transformation appropriate for general-elevation-angle scenarios is also incorporated. Secondly, a technique to detect sea surface oil spills using reflections from Global Navigation Satellite System (GNSS) satellites is presented. This technique is implemented by compensating the distortion induced during the DDM deconvolution process of scattering coefficient retrieval and employing the spatial integration approach (SIA) to retrieve the scattering coefficients unambiguously using the DDMs obtained by two separate antenna beams. A performance characterization including retrieval accuracy and resolution is demonstrated with respect to the signal-to-noise ratio and the size of oil slicks, respectively. Simulation based on the oil slick distribution of the Deepwater Horizon oil spill accident shows that the retrieval error can be reduced by the SIA after the distortion correction. The technique proposed here can be used to map oil slick extent on the ocean surface or it may be applied generically to produce physical surface maps of the

bistatic scattering coefficient from multiple DDM's from a single space-based platform. Lastly, a novel method is presented to retrieve sea surface wind speed and direction by fitting the two-dimensional simulated GNSS-R DDMs to measured data. An 18-second incoherent correlation is performed on the measured signal to reduce the noise level. Meanwhile, a variable step-size iteration as well as a fitting threshold are used to reduce the computational cost and error rate of the fitting procedure, respectively. Unlike previous methods, all the DDM points with normalized power higher than the threshold are used in the least-square fitting. An optimal fitting threshold is also proposed. To validate the proposed method, the retrieval results based on a dataset from the United Kingdom Disaster Monitoring Constellation satellite are compared with the *in-situ* measurements provided by the National Data Buoy Center, and good correlation is observed between the two.

Acknowledgements

The author would like to thank the Faculty of Engineering and Applied Science for affording him the opportunity of conducting this work. Particularly, the supervision provided by Dr. Weimin Huang and the patience and encouragement that he has shown throughout the research period are greatly appreciated. His suggestions and insights regarding the fundamentals of this topic have been invaluable.

The author would also like to thank Dr. Scott Gleason for sharing his work of GNSS-R Software Receiver, without which this research could not have been conducted properly. His suggestions at various stage of this work have been very helpful, too. The author also wishes to thank the Surrey Satellite Technology Ltd (SSTL), in particular Dr. Martin Unwin for providing GNSS-R measured data.

The author is grateful for financial support in the forms of a Research and Development Corporation (RDC) IRIF Ignite grant and a Natural Sciences and Engineering Research Council of Canada Discovery Grant to Dr. W. Huang.

Finally, the author deeply appreciates the understanding and patience of the author's parents, Mr. Zhengren Li and Mrs. Zhiling Song. This work could not be completed without their support.

Table of Contents

List of Tables

List of Figures

Table of Acronyms

The page numbers here indicate the place of first significant reference.

GNSS-R :	Global Navigation Satellite System-Reflectometry (abstract).
DDM :	Delay Doppler Map (abstract).
Z-V :	Zavorotny-Voronovich (abstract).
GNSS :	Global Navigation Satellite System (abstract).
SIA :	Spatial integration approach (abstract).
SAR :	Synthetic-aperture radar (p. 2).
CYGNSS :	Cyclone Global Navigation Satellite System (p. 4).
GPS :	Global Positioning System (p. 4).
SSTL :	Surrey Satellite Technology Limited (p. 4).
UK-DMC :	United Kingdom Disaster Monitoring Constellation (p. 4).
PRN :	Pseudo-random noise (p. 5).
LS :	Least-squares (p. 5).
DD :	Delay-Doppler (p. 5).
SP :	Specular point (p. 6).

HPBW : Half power beam width (p. 7).

C/A : Coarse/acquisition (p. 12).

ECEF : Earth-Centered, Earth-Fixed (p. 14).

ECXI : Earth-Centered, X-Z Incidence (p. 17).

ENU : East-North-Up (p. 17).

PDF : Probability density function (p. 22).

MSS : Mean-square slope (p. 22).

WS : Wind speed (p. 23).

WAF : Woodward ambiguity function (p. 24).

MODIS : Moderate Resolution Imaging Spectroradiometer (p. 25).

CLS : Constrained least squares (p. 31).

IGS : International GNSS Service (p. 41).

NDBC : National Data Buoy Center (p. 75).

Table of Symbols

The page numbers here indicate the place of first significant reference. Although not all symbols are explicitly referenced below, their definitions are obvious from the context.

τ_c : The length of a chip of the C/A code = 1 ms/1023 (p. 12).

σ^0 : Scattering coefficient (p. 12).

$\vec{\rho}$: Position vector of a surface point relative to specular point (p. 12).

D : Antenna radiation pattern (p. 12).

R_R : Distance from the GNSS-R receiver to a point on the ocean surface (p. 12).

R_T : Distance from the transmitting satellite to a point on the ocean surface (p. 12).

T_i : Coherent integration time (p. 12).

A : Glistening zone (p. 12).

$\langle |Y(\Delta\tau, \Delta f)|^2 \rangle$: Power expression of received signal (p. 12).

$\Delta\tau$: $\Delta\tau = \tau(\vec{\rho}) - \tau$ where τ and $\tau(\vec{\rho})$ are the C/A delay of specular point and the observed surface point, respectively (p. 12).

Δf : $\Delta f = f_d(\vec{\rho}) - f_d$ where f_d and $f_d(\vec{\rho})$ are the Doppler frequency of the specular point and the observed surface point, respectively (p. 12).

$S(\Delta f)$: Sinc function $S(\Delta f) = \sin(\pi T_i \Delta f)/(\pi T_i \Delta f)$ (p. 12).

$\Lambda(\Delta\tau)$: Triangle function $\Lambda(\Delta\tau) = 1 - |\Delta\tau|/\tau_c$ if $|\Delta\tau| < \tau_c$, and $\Lambda(\Delta\tau) = 0$ elsewhere (p. 12).

$\vec{S}$: Specular vector, the vectors from the earth center to the SP in the ECEF coordinate system (p. 14).

$\vec{S}_{old}$: First-guessed specular vector in the ECEF coordinate system (p. 15).

$\vec{d_S}$: The modification vector for $\vec{S}$ in the ECEF coordinate system (p. 15).

$\vec{S}_{temp}$: An intermediate vector for $\vec{S}$ in the ECEF coordinate system (p. 15).

$\vec{R}$: The vectors from the earth center to the receiver in the ECEF coordinate system (p. 15).

$\vec{T}$: The vectors from the earth center to the transmitter in the ECEF coordinate system (p. 15).

r : The radius of the Earth (p. 16).

t_s : Threshold for the modification vector (p. 16).

$\vec{S}_{new}$: Updated value for the specular vector in the ECEF coordinate system (p. 16).

λ_s : Longitude of the SP (p. 17).

φ_s : Latitude of the SP (p. 17).

$\vec{V}_{R_h}$, $\vec{V}_{T_h}$: Horizontal components of the velocities of receiver and transmitter, respectively, in the ENU System, (p. 17).

$\vec{V}_{R_n}$, $\vec{V}_{T_n}$: Velocities of receiver and transmitter in the ECXI System, respectively (p. 18).

$\vec{T}_n$, $\vec{R}_n$: Vectors from the earth center to the transmitter and receiver, respectively, in the ECXI System (p. 18).

$\vec{S}_n$: Position vector of the specular point in the ECXI system (p. 19).

$\vec{V}_R$: Velocity of the receiver in the ECXI System (p. 19).

$\vec{V}_T$: Velocity of the transmitter in the ECXI System (p. 19).

$\vec{V}_S$: Velocity of a grid element in the ECXI System (p. 19).

c : The speed of electromagnetic waves (p. 20).

f_l : The L1 carrier frequency = 1575.42 MHz (p. 20).

$\hat{n}$: Unit vector of the scattered wave (p. 20).

$\hat{m}$: Unit vector of the incident wave (p. 20).

f : Frequency of C/A code = 1.023 $\times 10^6$ Hz (p. 21).

$|\Re|^2$: The Fresnel reflection coefficient (p. 21).

$P(\cdot)$: Probability density function of the ocean surface slope (p. 22).

k : Carrier wave number (p. 22).

$\vec{q}$: Scattering vector $\vec{q} \equiv k(\hat{n} - \hat{m}) \equiv \vec{q}_\perp + q_z \hat{z}$ (p. 22).

$\vec{s}$: Ocean surface slope (p. 22).

s_x : The surface slope component along the x axis in the ECXI coordinate system (p. 22).

s_y : The surface slope component along the y axis in the ECXI coordinate system (p. 22).

φ_0 : The angle between the wind direction and the x-axis (p. 22).

$\sigma_{u,c}$: Upwind mean-square slope component for clean sea surfaces (p. 22).

$\sigma_{c,c}$: Crosswind mean-square slope component for clean sea surfaces (p. 22).

$\sigma_{u,s}$: Upwind mean-square slope component for oil-slicked sea surfaces (p. 23).

$\sigma_{c,s}$: Crosswind mean-square slope component for oil-slicked sea surfaces (p. 23).

U_{10} : Wind speed (WS) at 10 m height above sea level (p. 23).

$\chi(\Delta\tau, \Delta f)$: Woodward ambiguity function (WAF) (p. 24).

Σ : Deblurred DDM, i.e., the reflected signal power without considering the Woodward ambiguity function (p. 24).

N : Additive thermal noise (p. 31).

Σ_γ : Retrieval result of the deblurred DDM (p. 32).

p : Second order Laplacian operator (p. 32).

γ : Weight parameter of p (p. 32).

$H_{0\gamma}$: The distortion distribution of a clean ocean surface (p. 33).

$|J(\cdot)|$: The determinant of the Jacobian matrix (p. 39).

SNR_p : The processed signal-to-noise ratio (p. 44).

$\langle |Y_N|^2 \rangle$: Noise power of DDMs (p. 46).

α : Relative error of the scattering coefficient retrieval result (p. 48).

σ°_γ : The retrieved scattering coefficients (p. 48).

ΔR_τ : The delay resolution (p. 49).

ΔR_f : The Doppler resolution (p. 49).

A_s : The area of an oil spill (p. 62).

V : The volume of the spill (barrel) (p. 62).

t : Oil spill duration time (min) (p. 62).

ρ_0 : Density of the oil layer (p. 62).

$\Delta\rho$: Density difference between water and oil (p. 62).

$F1$, $F2$: The relative flat regions shown in the reference map of the GNSS-R dataset collected over land (p. 64).

$R1$, $R2$: The relative rough regions shown in the reference map of the GNSS-R dataset collected over land (p. 64).

$\varepsilon(\cdot)$: Least square cost function (p. 69).

$f(U_{10})$: Empirically modified wind speed for mean square slope model(p. 69).

τ_m : Offset of C/A delay (p. 69).

f_m : Offset of Doppler frequency shift (p. 69).

a : Scaling factor for fitting the modelled DDM magnitude to that of the measured DDM (p. 70).

T_a : Pre-defined value to terminate the iteration for a (p. 70).

Chapter 1

Introduction

1.1 Research Rationale

The increasing interest in Earth surface information leads to the corresponding need for accurate and quick remote sensing approaches. Invented 60 years ago, radar systems have been widely used to meet this demand. Existing radars can be grouped according to their carriers and whether they are based on active or passive radiation [1]. There are land-based, air-based and space-based radars that use either active or passive sources. Each radar category has its own cost, flexibility, accuracy, spatial and temporal coverage. Generally, land-based radars have lower cost, and air-based radars are more flexible. Most space-based sensing techniques use low-earth-orbit satellite to carry the transmitting and receiving antenna systems. Hence, the receiver for a space-based system has high altitude and large observing area [2]. The swath width of such systems is typically from hundreds to thousands of kilometers (km) depending on the antenna footprint. As a result, in order to achieve accurate and quick earth surface information on a global scale, space based sensors become a reasonable choice due to their high spatial and temporal coverage. Typical remote sensing parameters

using this type of sensors include wind speed [3–5], sea ice [6–12], soil moisture [13], brightness temperature [14] and surface roughness [15, 16].

Although the space-based systems hold the potential to provide global remote sensing, existing techniques have their limitations. Sensors operating at very high frequencies, such as the radiometers and imaging cameras, will have a difficulty "looking" through the atmosphere especially when there are clouds [17]. Another commonly used sensor is synthetic-aperture radar (SAR). It usually has high cost because of its relatively complex instruments (transmitters and receivers) and the need of large constellations. In the last two decades, Global Navigation Satellite System Reflectometry (GNSS-R), a new technique that passively measures scattered signals from GNSS has been used for remote sensing Earth surface characteristics. Unlike imaging satellite, which typically operate at 3.8×10^5 GHz frequency, the GNSS-R uses microwave signals. Thus, it can provide Earth surface monitoring under a wider range of weather conditions with/without clouds. Without the cost of transmitters, GNSS-R uses relatively cheap and simple instruments. Hence, the research in this thesis focuses on remote sensing using GNSS-R.

It is well known that electromagnetic radiation scattered from the ocean surface contains statistical information regarding the surface properties [18, 19]. This relationship forms the basis of oceanic radar remote sensing systems. Thus, in order to determine surface properties, this surface scattering mechanism must be investigated. Namely, the process to determine scattering coefficients using collected GNSS-R signals needs to be developed.

It is known that the nature of the scattered signals depends on the operating frequency, antenna beam width, polarization, as well as the system configuration (monostatic or bistatic). The model (Z-V model, see Section 1.2) that formulates scattering signals under different surface conditions already exists. Since the mea-

sured signal and the geographic position are not on an one-to-one relationship, the parameter retrieval process is significantly complicated. A relatively mature GNSS-R sensing approach involves matching measured signals to signals simulated under different surface conditions. Despite its high computational cost, this approach is generally suitable for surfaces with little slope variations such as clean ocean surfaces with spatially consistent wind fields. However, for other surface conditions such as oil slicked sea surfaces or land surfaces, it will be challenging to use this approach for remote sensing. In an attempt to solve this problem, the scattering coefficient retrieval process is investigated here. Rather than estimating spatially averaged sea state parameters over the whole observed ocean region, the proposed method is used to determine the scattering coefficient distribution over the observed area in a more effective and efficient way and has the potential to greatly increase the retrieval accuracy for surfaces with highly varied slopes. In other words, it can be applied to not only clean ocean surfaces, but also surfaces such as oil slicked ocean surfaces and land surfaces.

One of the most investigated sea parameters is the sea-surface wind field, which in turn is very useful for a number of meteorological and oceanographic applications. For example, surface wind helps weather forecasting. As weather disturbances occur over the oceans, sea surface wind observations can help improve the prediction of such disturbances [20,21]. Moreover, surface winds may be used to drive surface wave and surge models for wave and ocean modelling [22–24]. Furthermore, the surface wind field is required for validating ocean atmosphere global models, which in turn are essential to the understanding of the Earth climate [25]. Therefore, this research investigates the sea surface wind field retrieval using GNSS-R.

Another application for GNSS-R investigated in this research is oil slick detection. Marine pollution caused by oil spill has always been a serious threat to the ocean

environment. In the 2010 Macondo incident in the Gulf of Mexico, a total oil discharge of 210 million gallons was estimated, forming a 200 km^2 "kill zone" of marine life surrounding the blown well [26]. In the case of large accidents like this, scattering coefficient retrieval has the potential to detect the spill, monitor its extent and track its spreading trend at a relatively low-cost. Therefore, in this research the GNSS-R remote sensing methodology is investigated not only for clean ocean surfaces (wind field retrieval) but also for oil contaminated surfaces (oil slick detection).

It is desired that the retrieval approach developed here should also provide a foundation for the further investigation of GNSS-R remote sensing for land surfaces properties and cyclones.

1.2 Literature Review

During the past 20 years, the signals transmitted from the GNSS have been demonstrated to be not only capable of providing navigation and location services, but also to be useful in conducting remote sensing missions [27–30]. This technique, which is commonly referred to as the Global Navigation Satellite System-Reflectometry, was first proposed by Martin-Neira as an innovative approach for ocean altimetry [31]. The advantage of GNSS is primarily the improved coverage using a relatively cheap and simple instrument. Also, such systems may be launched in small constellations, as in NASA's Cyclone Global Navigation Satellite System (CYGNSS) mission. The first space-based detection of an ocean-reflected Global Positioning System (GPS) signal was achieved by researchers at NASA's Jet Propulsion Laboratory [27]. Subsequently, the Surrey Satellite Technology Limited (SSTL) launched the United Kingdom Disaster Monitoring Constellation (UK-DMC) satellite in 2003 [5]. This passive GPS bistatic radar experiment has collected a large amount of space-based data over

ocean, land and ice surfaces. A large number of GNSS transmitters provide high temporal sampling rate and global coverage, making the GNSS-R technique suitable for measuring highly varying parameters, such as scattering coefficients and sea surface wind fields.

In 1998, the possibility of remote sensing sea surface roughness was first presented by Garrison *et at.* [32], and a preliminary experimental measurement was provided. The technique proposed in [32] provided a good foundation for GNSS-R remote sensing by using a bistatic geometry with existing sources of radio frequency illumination as well as the correlation properties of the pseudo-random noise (PRN) signal transmitted by GPS.

In 2002, the retrieval of wind speed and direction using GNSS-R was first investigated in [33] using multiple scattered signals collected using an air-borne based instrument. In that work two techniques were studied. The first recognized that the most significant information in the reflected signal is contained in the trailing edge slope of the waveform. The second attempted to match the complete shape of the waveform. Basically, both of the approaches are based on the least-squares (LS) fitting technique and try to fit the measured delay waveform at a single Doppler frequency to theoretically modelled waveforms; therefore, this method is hereafter referred to as one-dimensional LS fitting. The wind velocity that best matches the detected signal waveform is regarded as the optimal one. This approach has been validated using the data from two campaigns of aircraft flights [33]. However, considering the relative small amount of air-based verification data, the robustness of this approach may not be satisfactory especially when applied to space-based experiments. In 2011, another approach for wind retrieval was presented [34] using the scattering coefficient distribution based on the relationship between the spatial and the delay-Doppler (DD) domain. Rather than assuming a uniform distribution of wind, this approach pro-

vided a wind speed value for each spatial point in the glistening zone. Although the result obtained using this approach is informative in terms of wind speed, it lacks the wind direction information. Moreover, this approach requires more knowledge of the remote sensing system such as the magnitude of the incident GPS signal as well as the parameters of the receiver (amplifiers, automatic gain control) [16]. In 2013, another approach [35] was proposed that directly links the DDM observables with wind speeds through a linear regression. A clear correlation was observed between the two parameters according to the data collected from air campaigns, and reasonably good results were retrieved. However, none of these approaches shows very satisfying and robust results. More importantly, they lack the proper tests that involve real space-based GNSS-R data, rendering them inappropriate for application in real-world applications.

Another important application for GNSS-R remote sensing is the recently proposed oil slick detection. The possibility of detecting oil slicks on sea surfaces using this technique was investigated by Valencia *et al.* [36,37]. This research was based on the fact that the scattering coefficients of slick-covered surfaces are different from those of slick-free surfaces under similar wind conditions. Hence, the oil slicked area could be detected by retrieving the scattering coefficient distribution from the scattered signal waveforms, known as delay-Doppler maps (DDM). Although the preliminary demonstration of this novel oil-slick detection approach showed promise, there were still several limitations that impede the detection process from being applied to real GNSS-R datasets. The first limitation is the surface ambiguity problem which refers to the ambiguous relationship between the DDM points and spatial points. One solution for this problem is tilting the beam of the receiver antenna away from the specular point (SP) to form a spatial filter [36]. With this filter, only one of the two ambiguity-free zones is used to generate a DDM, thus eliminating the spatial ambiguity. However,

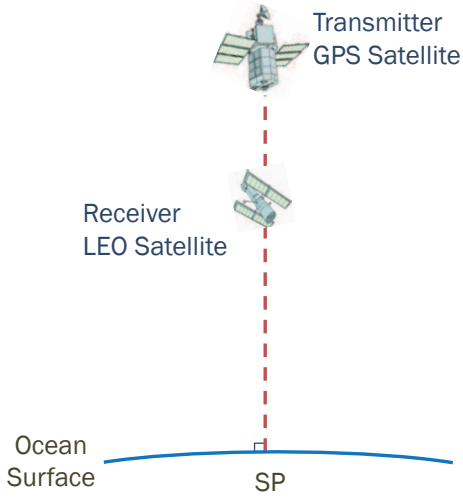

Figure 1.1: A special scenario with grazing angle of 90°.

the use of spatial filtering assumes a significant difference between the power received from the two ambiguity-free zones so that the power from the more remote zone can be ignored. Still, in some GNSS-R satellite missions, the pointing angle and beam width of the antenna may not permit this spatial filtering. For example, the UK-DMC satellite carried a non-steerable antenna, offset by an angle of 10° along track and had a corresponding half power beam width (HPBW) of 28° [5]. This indicates that the HPBW footprint would lie across both zones. Hence, the power contribution from the more remote zone will induce errors for the datasets obtained by GNSS-R antennas with relatively large surface footprints [5, 38]. The second limitation is that the existing oil slick detection algorithm was conducted only in a simplified scenario with a grazing angle of 90° based on simulation. This indicates that the sub-satellite points, at which a line between the satellite and the centre of the Earth intersects the Earth surface, of the GPS satellite (transmitter) and LEO satellite (receiver) are overlapped with each other at the SP as shown in Fig.1.1. However, this will rarely be the case in practical situations, where the reflections may be observed from a range of grazing angles. To take full advantage of the spatial resolution capabilities provided by GNSS-R, it is desirable that all visible reflection points are used. Finally, the

original oil-slick detection used the Jacobian approach during the retrieval process, and the corresponding result showed relatively low accuracies near the ambiguity free line [36]. Although the Jacobian approach has the advantage of less computational cost for modelling DDMs [39], due to the surface mapping approximations involved it is subject to higher error rates (with errors as high as 20% when applied to scattering coefficient retrieval under the coherent integration time of 10 ms [36]).

1.3 The Scope of the Thesis

As was discussed in Section 1.2, the primary content of this thesis includes the enhancement of the techniques for sea surface oil slick detection and ocean surface wind field retrieval from GNSS-R signals. With a view to mitigating the limitations of existing wind retrieval approaches, a novel method is presented to retrieve sea surface wind speed and direction by fitting the two-dimensional simulated GNSS-R DDMs to measured data. An optimal fitting threshold is employed to determine the DDM points that will be used for the fitting process. In order to verify this approach, three space-based GNSS-R datasets collected by the UK-DMC satellite are employed.

With respect to oil slick detection, this research presents several major modifications in the detection approach to reduce the limitations of the original method [37] discussed in Section 1.2. To solve the ambiguity problem, a configuration is proposed involving two antenna beams over the same area of interest. While this method was first proposed in [40] to eliminate the ambiguity for wind speed retrieval, this research applies the method to oil slick detection. In order to enhance the oil slick detection system for different geometries, this research discusses the method to simulate and detect oil slicks using general geometric scenarios as shown in Fig. 1.2. In this figure, V is the sub-satellite point of the receiver. Moreover, a spatial integration approach

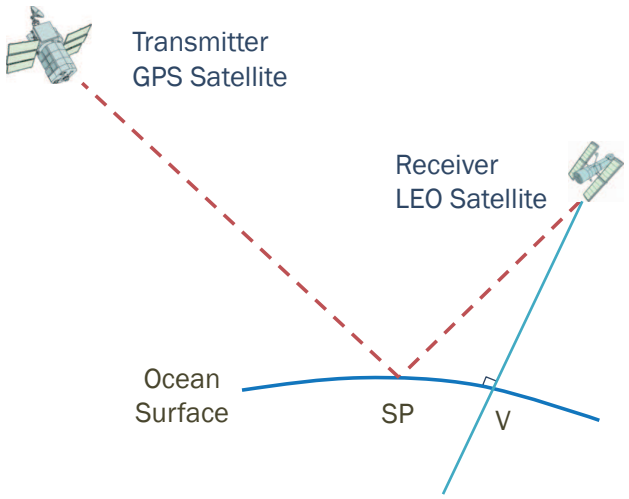

Figure 1.2: General scenario.

(SIA) [41] is employed to provide a more robust integration of the surface. In addition, a method to correct the distortions induced during the DDM deconvolution is used to improve the accuracy of the scattering coefficient retrieval. The performance of the proposed technique is also characterized under different noise levels. Finally, this scattering coefficient retrieval technique is validated using both a a real space-based GNSS-R dataset collected over land surfaces.

The thesis is organized as following:

In Chapter 2, the detailed process to generate the DDM of oil-slicked sea surfaces under general geometry is presented. This process, particularly the GNSS scattering model and scattering coefficient model within it, forms the theoretical foundation of the rest of the research in this thesis.

Chapter 3 presents the new oil slick detection approach i.e., the SIA by employing the slicked sea surface DDM under a general scenario as discussed in Chapter 2. The detailed steps for retrieving the scattering coefficient as well as the major modifications of the original detection method are described here. A preliminary verification is conducted using both a simulated DDM and a real DDM dataset collected over land surfaces.

Chapter 4 contains a discussion of the new wind retrieval approach, in which a 2-dimensional least-square fitting is employed to match the simulated DDMs with the measured one.

In Chapter 5, the fundamental conclusions from the previous three chapters are summarized. A few suggestions for the future work are also provided.

Chapter 2

DDM Simulation of Oil Slicked Sea Surface under General Scenario

In this chapter, the detailed process to simulate GNSS-R DDMs of oil slicked sea surfaces under general scenarios is presented. More specifically, the particulars of how to extend the simulation process from a simplified scenario to general scenarios are discussed. The chapter is organized as follows: Section 2.1 briefly introduces the theory of DDM simulation. Section 2.2 describes the glistening zone determination and mapping power distribution from the spatial domain to the DD domain. In Section 2.3, the simulation results under the simplified scenario and general scenario are compared and discussed. Finally, a general chapter summary is presented in Section 2.4.

2.1 Basic Theory of DDM Simulation

Delay Doppler Maps depict the power distribution of the signals scattered from the glistening zone in the DD domain using the GNSS Z-V scattering model [42]. It is

expressed as

$$\left\langle |Y(\Delta\tau, \Delta f)|^2 \right\rangle = T_i^2 \iint_A \frac{D^2(\vec{\rho})\sigma^0(\vec{\rho})\Lambda^2(\Delta\tau)|S(\Delta f)|^2}{4\pi R_R^2(\vec{\rho})R_T^2(\vec{\rho})} d^2\rho \tag{2.1}$$

with the following definitions

σ^0	scattering coefficient;
$\vec{\rho}$	position vector of a surface point relative to specular point;
D	antenna radiation pattern;
R_R	distance from the GNSS-R receiver to a point on the ocean surface;
R_T	distance from the transmitting satellite to a point on the ocean surface;
T_i	coherent integration time;
A	glistening zone;
$\langle \lvert Y(\Delta\tau, \Delta f)\rvert^2 \rangle$	power expression of received signal;
$\Delta\tau = \tau(\vec{\rho}) - \tau$	τ and $\tau(\vec{\rho})$ are the C/A delay of specular point and the observed surface point, respectively;
$\Delta f = f_d(\vec{\rho}) - f_d$	f_d and $f_d(\vec{\rho})$ are the Doppler frequency of the specular point and the observed surface point, respectively.

The triangular pulse function Λ is defined as $\Lambda(\Delta\tau) = 1 - |\Delta\tau|/\tau_c$ if $|\Delta\tau| < \tau_c$, and $\Lambda(\Delta\tau) = 0$ elsewhere. $\tau_c = 1$ ms/1023 is the length of a chip of the coarse/acquisition (C/A) code which is used as the PRN code by the GPS signals. The function $S(\Delta f)$ is defined as $S(\Delta f) = \sin(\pi T_i \Delta f)/(\pi T_i \Delta f)$. The observed area A is approx-

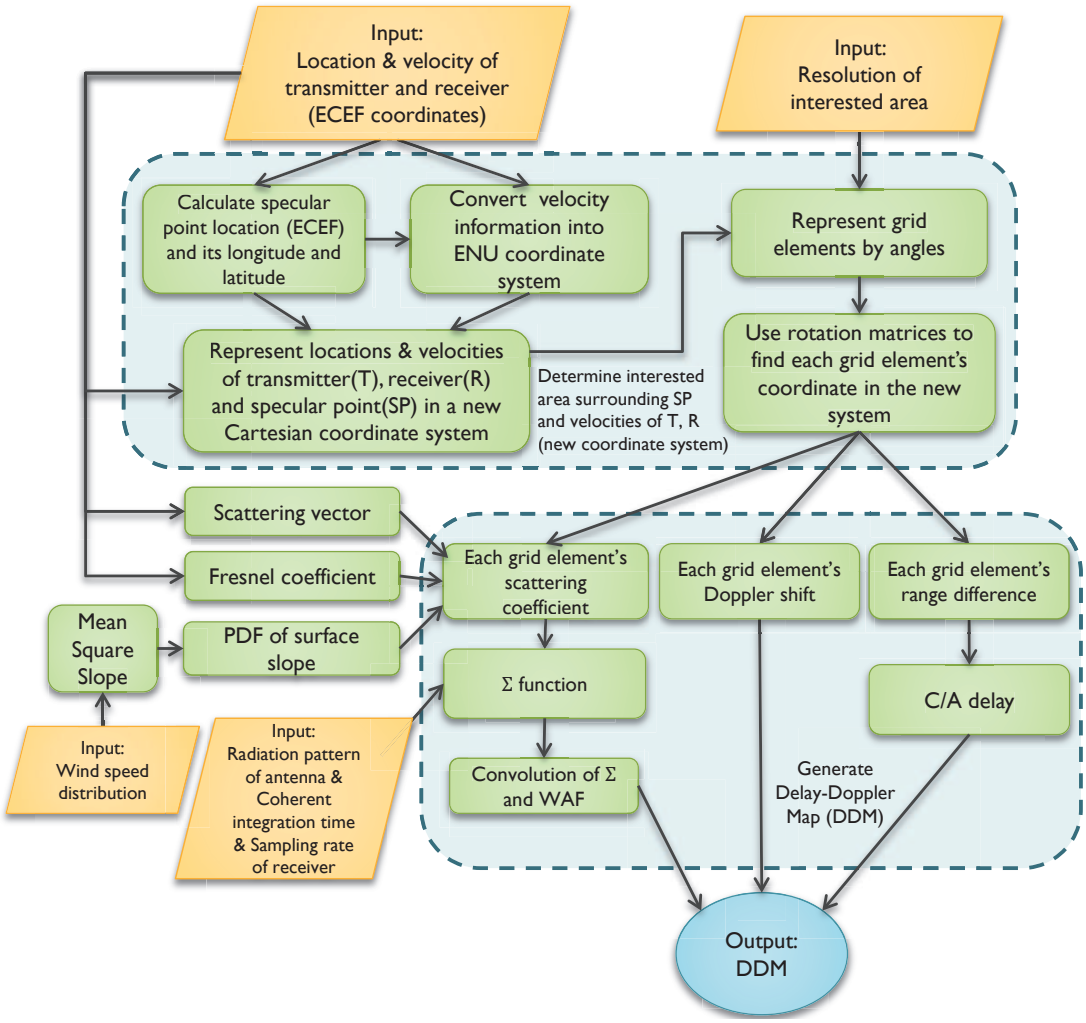

Figure 2.1: Flow chart of DDM simulation.

imately the glistening zone, which is determined by the area that scatters enough power to be detected by the GNSS-R receiver.

As can be seen in Eq. (2.1), in order to generate a DDM, the location and scope of A needs to be determined first. Secondly, since grid elements are on the spherical surface of the earth, an accurate way is required to obtain their coordinates. The third step is to determine the relationship between spatial domain $\vec{\rho}$ and the DD domain $(\Delta\tau, \Delta f)$. Then, the DDM may be simulated using Eq. (2.1). A more detailed process can be seen in the flow chart in Fig. 2.1.

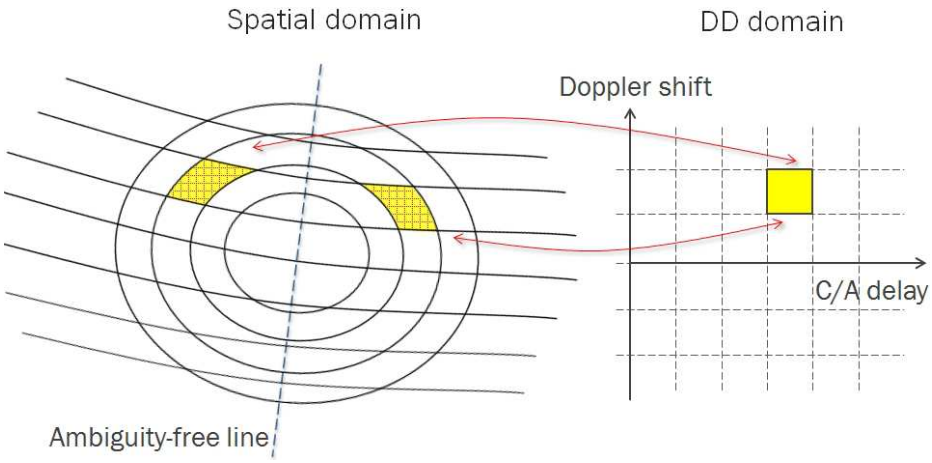

Figure 2.2: Relationship between the spatial clusters and DD points.

2.2 Detailed Methodology of DDM Simulation

This section explains the detailed DDM simulation process which includes three steps: 1) determining the location of the glistening zone surrounding the specular point (SP) in the Earth-Centered, Earth-Fixed (ECEF) coordinate System [43]. 2) obtaining the coordinates of the grid elements (defined in Fig. 2.2) in this glistening zone. 3) mapping the power scattered from glistening zone into the DD domain. The first two steps constitute the main process in extending the simplified scenario to a general scenario.

2.2.1 Specular Point Determination in the ECEF System

For GNSS-R, the glistening zone always surrounds the SP. Therefore, the position of the glistening zone could be obtained by determining the SP. The location of the SP can be obtained with the steps shown in Fig. 2.3. More specific steps of this algorithm are discussed below.

In this process, all the coordinates are denoted in the ECEF system. $\vec{S} = [X_S, Y_S, Z_S]$ denotes the vector from the center of the earth to the SP. In order to get

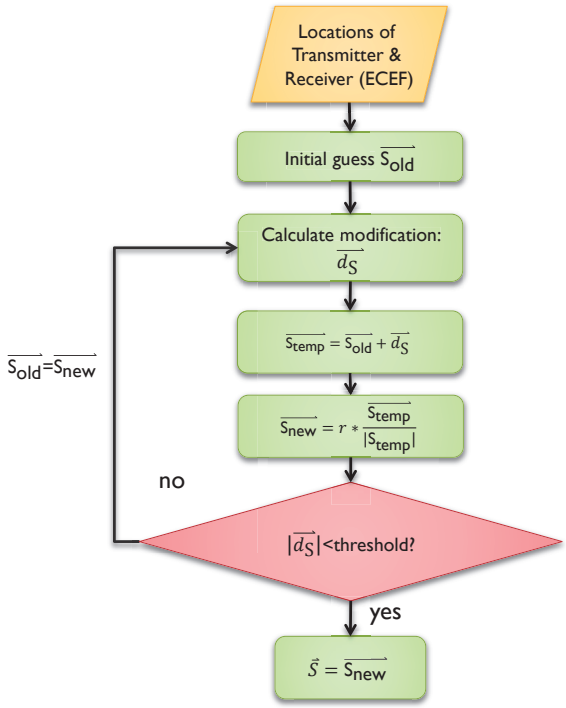

Figure 2.3: Flow chart of determining SP.

the SP, the initial guess of its location is assumed to be on the sub-satellite point of the receiver, i.e., point V in Fig. 1.2. Using this initializing specular vector, $\vec{S}_{old}$, an iterative updating process, employing a modification vector $\vec{d_S}$ (Eq. 2.2), is implemented to update $\vec{S}_{old}$. The modification vector is the summation of two normalized vectors and is given by [7]

$$\vec{d_S} = \frac{\vec{T} - \vec{S}_{old}}{\left|\vec{T} - \vec{S}_{old}\right|} + \frac{\vec{R} - \vec{S}_{old}}{\left|\vec{R} - \vec{S}_{old}\right|} \tag{2.2}$$

where $\vec{T}$, $\vec{R}$ and $\vec{S}_{old}$ represent the vectors from the centre of the earth to the transmitter, receiver and SP in the ECEF coordinate system, respectively. $\vec{T} - \vec{S}_{old}$ indicates the incoming vector from the transmitter to the temporary SP, and $\vec{R} - \vec{S}_{old}$ indicates the reflected vector from the temporary SP to the receiver. An intermediate vector is obtained as $\vec{S}_{temp} = \vec{S}_{old} + \vec{d_S}$. To ensure the new SP location is on the earth's surface

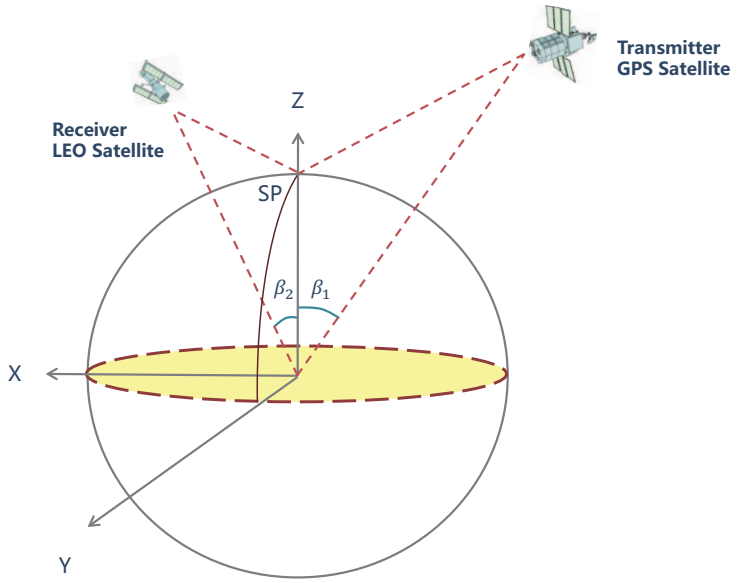

Figure 2.4: Earth-centered, X-Z incidence coordinate system.

after updating, the corrected SP vector must be scaled by the radius of the earth, r. Then, the new SP can be obtained using $\vec{S}_{new} = r\hat{S}_{temp}$ where $\hat{S}_{temp}$ is the unit vector of $\vec{S}_{temp}$. Finally the magnitude of the modification vector $\vec{d_S}$ will be less than a threshold t_s which is pre-defined according to the demand of the location accuracy of SP. When $|\vec{d_S}| < t_s$, the position of SP is considered to be found. This position is the center of the glistening zone.

2.2.2 Coordinates Transformation from ECEF to ECXI System

This section defines a new Cartesian coordinate system which may be used to reinterpret the coordinates of the transmitter and receiver, and it will facilitate the calculation of the grid element coordinates. This system has its origin at the center of the earth. The SP is along the z axis, the x-y plane is parallel to the plane tangent to the surface at the SP, and the x and z axes are in the incidence plane (see Fig. 2.4). In

the following paragraphs this coordinate system is referred to as the Earth-Centered, X-Z Incidence (ECXI) system. In order to determine the ECXI coordinates of the grid elements, two steps are required: 1) the locations and velocities of the transmitter and receiver must be transformed from the ECEF coordinate system to the ECXI system; 2) the coordinates of the grid elements must be calculated.

2.2.2.1 Transmitter and Receiver in the ECXI System

In order to facilitate the process of determining the coordinates of the grid elements of the ocean surface, both the locations and velocities of the transmitter and receiver need to be transformed to the ECXI system. To represent the velocities of the transmitter and receiver in the ECXI system, intermediate velocities in a East-North-Up (ENU) system [43] centred at the SP are calculated first. The conversion of the velocity from the ECEF to the ENU coordinate system is given as

$$\begin{bmatrix} V_{x,enu} \\ V_{y,enu} \\ V_{z,enu} \end{bmatrix} = \begin{bmatrix} -\sin\lambda_s & \cos\lambda_s & 0 \\ -\sin\varphi_s\cos\lambda_s & -\sin\varphi_s\sin\lambda_s & \cos\varphi_s \\ \cos\varphi_s\cos\lambda_s & \cos\varphi_s\sin\lambda_s & \sin\varphi_s \end{bmatrix} \begin{bmatrix} V_{x_{ecef}} \\ V_{y_{ecef}} \\ V_{z_{ecef}} \end{bmatrix} \tag{2.3}$$

where λ_s and φ_s are the longitude and latitude of the SP, respectively. By applying the ECEF velocities in Eq. (2.3), the transmitter's ENU velocity $\vec{V}_{T_{enu}}$ and receiver's ENU velocity $\vec{V}_{R_{enu}}$ will be obtained. Converting the velocities into the ECXI system requires the horizontal components of the velocities $\vec{V}_{R_h} = [V_{R_{x,enu}}, V_{R_{y,enu}}]$ and $\vec{V}_{T_h} = [V_{T_{x,enu}}, V_{T_{y,enu}}]$. Next, the angles between the y axis and the velocity vectors $\vec{V}_{R_h}$ and $\vec{V}_{T_h}$ are found as $\theta_{V_R} = \tan^{-1}(V_{R_{x,enu}}/V_{R_{y,enu}})$ and $\theta_{V_T} = \tan^{-1}(V_{T_{x,enu}}/V_{T_{y,enu}})$, respectively. A similar method may be used to determine the angle θ_r between the y axis and the horizontal component of the displacement vector from the receiver to the

transmitter: $\vec{u}_h = [u_x, u_y]$, where $\vec{u} = \vec{T}_{enu} - \vec{R}_{enu}$. Then the angle between $\vec{u}_h$ and velocities $\vec{V}_{R_h}$ and $\vec{V}_{T_h}$ can be obtained by $\Delta\theta_R = \theta_{V_R} - \theta_r$, $\Delta\theta_T = \theta_{V_T} - \theta_r$. Finally, the velocities can be converted into the ECXI system as

$$\vec{V}_{R_{ecxi}} = [|V_{R_h}|\cos(\Delta\theta_R), |V_{R_h}|\sin(\Delta\theta_R), V_{R_{z,enu}}] \tag{2.4}$$

$$\vec{V}_{T_{ecxi}} = [|V_{T_h}|\cos(\Delta\theta_T), |V_{T_h}|\sin(\Delta\theta_T), V_{T_{z,enu}}]. \tag{2.5}$$

Converting the locations of transmitter and receiver to the ECXI system can be performed with the following steps: Given that $\hat{R}$, $\hat{T}$ and $\hat{S}$ are the unit vectors from the earth center to the transmitter, receiver and SP, respectively, in the ECEF coordinate system, the angle β_1 and β_2 can be obtained by: $\beta_1 = \cos^{-1}(\hat{T} \cdot \hat{S})$ and $\beta_2 = \cos^{-1}(\hat{R} \cdot \hat{S})$. Then, in the ECXI system, $\vec{T}$ and $\vec{R}$ become

$$\vec{T}_n = [-|T|\sin(\beta_1), 0, |T|\cos(\beta_1)] \tag{2.6}$$

$$\vec{R}_n = [|R|\sin(\beta_2), 0, |R|\cos(\beta_2)]. \tag{2.7}$$

In the following paragraphs, all the vectors are designated in terms of the ECXI coordinate system.

2.2.2.2 Grid Elements in the ECXI System

The glistening zone is a spherical surface because of the curvature of the earth. Therefore, each grid element in the ECXI system will be designated in terms of a pair of angles (θ_1, θ_2) as shown in Fig. 2.5. When determining coordinates of the grid elements in the ECXI system, the bounds of these pairs are defined by the width and length of the glistening zone in relation to the distance from the earth center. For example, if the glistening zone is a circular area with radius r_g, then the bound of

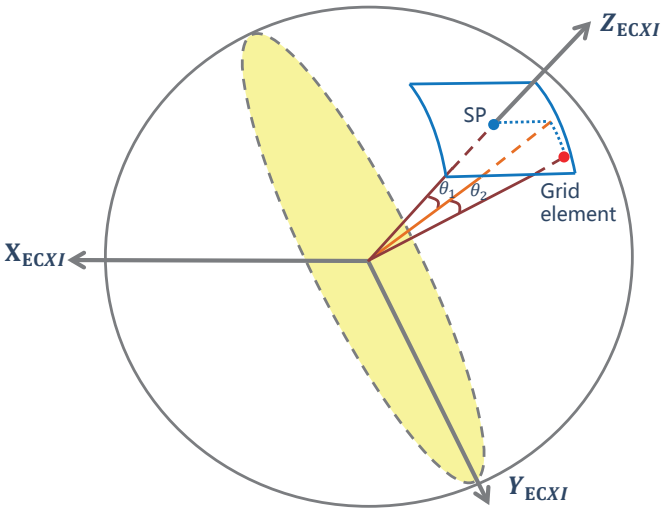

Figure 2.5: A grid element represented by the angles with respect to the SP in x and y direction, respectively. The blue dot indicates the SP and the red dot indicates the gird element.

θ_1 and θ_2 would be $\phi_1 = \frac{r_g}{|\vec{S}_n|}$ and $\phi_2 = \frac{r_g}{|\vec{S}_n|}$, respectively, where $\vec{S}_n = (0, 0, r)$ is the position vector of the SP in the ECXI system. In the process, the angle θ_1 ranges from $-\phi_1$ to ϕ_1 and the angle θ_2 ranges from $-\phi_2$ to ϕ_2. The position vector $\vec{\rho}(\theta_1, \theta_2)$ from the earth's center to grid element (θ_1, θ_2) in the ECXI system can be obtained by $\vec{\rho}(\theta_1, \theta_2) = \vec{S}_n M_1 M_2$ where the rotation matrix M_1 with respect to θ_1 is [44]

$$M_1 = \begin{bmatrix} -\cos(\theta_1) & 0 & \sin(\theta_1) \\ 0 & 1 & 0 \\ \sin(\theta_1) & 0 & \cos(\theta_1) \end{bmatrix} \tag{2.8}$$

and the rotation matrix M_2 with respect to θ_2 is

$$M_2 = \begin{bmatrix} 1 & 0 & 0 \\ 0 & \cos(\theta_2) & -\sin(\theta_2) \\ 0 & \sin(\theta_2) & \cos(\theta_2) \end{bmatrix}. \tag{2.9}$$

For simplicity, $\vec{\rho}(\theta_1, \theta_2)$ is referred hereafter as $\vec{\rho}$.

2.2.3 Power Distribution in the Spatial and DD Domains

Mapping the GNSS-R received power distribution from the spatial to the DD domain first involves the determination of the Doppler shift, C/A delay and scattering coefficient of each grid element.

2.2.3.1 Doppler Frequency Shift

The Doppler frequency shift f_d is caused by the relative motion between the transmitter, receiver and grid elements. It can be obtained using [7]

$$f_d(\vec{\rho}) = \frac{[(\vec{V}_S - \vec{V}_T) \cdot \hat{m}]f_l}{c} + \frac{[(\vec{V}_R - \vec{V}_S) \cdot \hat{n}]f_l}{c} + f_{clk} \tag{2.10}$$

where $\vec{V}_T$, $\vec{V}_R$ and $\vec{V}_S$ represent the velocity of transmitter, receiver and a grid element, respectively; f_l is the L1 carrier frequency = 1575.42 MHz; $\hat{n}$ is the unit vector of the scattered wave and $\hat{m}$ is the unit vector of the incident wave [44]. f_{clk} denotes the Doppler shift caused by the receiver clock drift, assumed here to be 0. In [45], it is shown that a time-evolving or dynamic ocean surface (grid element) will produce a non-zero Doppler shift. Here, the velocity of sea surface $\vec{V}_s$ has been assumed as zero since the magnitude of the grid element velocity is much smaller than the speed of the transmitter and receiver [7, 42]. Since the main purpose in this chapter is to investigate the oil slick effect on the GNSS DDM, the influence of a non-zero grid element speed is ignored for simplicity. For the SP, the frequency shift is

$$f_d = \frac{f_l}{c}(-\vec{V}_{Tn} \cdot \frac{\vec{S}_n - \vec{T}_n}{|\vec{S}_n - \vec{T}_n|} + \vec{V}_{Rn} \cdot \frac{\vec{R}_n - \vec{S}_n}{|\vec{R}_n - \vec{S}_n|}) \tag{2.11}$$

and then Δf in the variables explanation of Eq. (2.1) can be acquired using $f_d(\vec{\rho})$

and f_d.

2.2.3.2 C/A Delay

The C/A delay refers to the time delay of signals reflected from different grid elements as given by

$$\tau(\vec{\rho}) = \frac{f(R_\rho + T_\rho)}{c} \tag{2.12}$$

where R_ρ and T_ρ are the distances from the grid element to the receiver and transmitter, respectively; $f = 1.023 \times 10^6$ Hz is the frequency of the C/A code. For the SP, the C/A delay is

$$\tau = \frac{f}{c}(|\vec{R}_n - \vec{S}_n| + |\vec{T}_n - \vec{S}_n|) \tag{2.13}$$

and then $\Delta\tau$ in the variables explanation of Eq. (2.1) can be acquired using $\tau(\vec{\rho})$ and τ. With the knowledge of both the DD coordinate and spatial coordinate of each grid element, the relationship between the DD and spatial domain is thus obtained.

2.2.3.3 Scattering Coefficient Distribution

The power received from each grid element is closely related to its scattering coefficient distribution σ^0. The equation to determine scattering coefficient is [42]

$$\sigma^0 = \pi|\Re|^2(\frac{|\vec{q}|}{q_z})^4 P(-\frac{\vec{q}_\perp}{q_z}) \tag{2.14}$$

where $\Re$ is the Fresnel reflection coefficient of the observed area. For clean sea surfaces, it is determined by the polarization, the complex dielectric constant of sea water, and the local elevation angle [42]. For oil contaminated surfaces, $\Re$ denotes the reflection coefficient of the layered structure consisting of air, oil layer and sea water. It is a function of the thickness of the oil slick, the local incidence angle, the complex dielectric constant of sea water and oil, and the polarization mode of the incident and

scattered waves [46]. The scattering vector is defined as

$$\vec{q} \equiv k(\hat{n} - \hat{m}) \equiv \vec{q}_{\perp} + q_z \hat{z} \tag{2.15}$$

where k is the carrier wave number. This vector can be obtained from the locations of the transmitter, receiver and corresponding grid element. The quantity $-\frac{\vec{q}_{\perp}}{q_z}$ is the ocean surface slope, and, for simplicity, it is denoted as $\vec{s}$ hereafter. Then, the probability density function (PDF) $P(\vec{s})$ of the ocean surface slope is [44]

$$P(\vec{s}) = \frac{1}{2\pi\sqrt{det(M)}} \exp\left[-\frac{1}{2}\begin{pmatrix} s_x \\ \\ s_y \end{pmatrix}^{\mathrm{T}} M^{-1} \begin{pmatrix} s_x \\ \\ s_y \end{pmatrix}\right] \tag{2.16}$$

where matrix M is

$$M = \begin{pmatrix} \cos\varphi_0 & -\sin\varphi_0 \\ \\ \sin\varphi_0 & \cos\varphi_0 \end{pmatrix} \cdot \begin{pmatrix} \sigma_u^2 & 0 \\ \\ 0 & \sigma_c^2 \end{pmatrix} \cdot \begin{pmatrix} \cos\varphi_0 & \sin\varphi_0 \\ \\ -\sin\varphi_0 & \cos\varphi_0 \end{pmatrix} \quad . \tag{2.17}$$

In Eq. (2.16), $det(M)$ denotes the determinant of matrix M; s_x, s_y represent the surface slope components on the x and y axes, respectively, in the ECXI coordinate system [47, 48]. As shown in Fig. 2.4, this system has its origin at the center of the earth with the SP locating on the z axis. The x and z axes form the plane of incidence. In Eq. (2.17), φ_0 is the angle between the wind direction and the x axis [44]. It should be noted that there is a 180° ambiguity in φ_0 due to the symmetry of the surface slope PDF [16]. σ_u^2 and σ_c^2 indicate the upwind and crosswind mean-square slope (MSS) components respectively, which are given by Cox and Munk in [49] as

$$\begin{aligned} \sigma_{c,c}^2 &= 0.003 + 1.92 \times 10^{-3} U_{10} \\ \sigma_{u,c}^2 &= 3.16 \times 10^{-3} U_{10} \end{aligned} \tag{2.18}$$

$$\sigma_{c,s}^2 = 0.003 + 0.84 \times 10^{-3} U_{10}$$
$$\sigma_{u,s}^2 = 0.005 + 0.78 \times 10^{-3} U_{10} \tag{2.19}$$

where the second subscripts of the MSSs, i.e. c and s, stand for "clean" and "slick", respectively. U_{10} denotes the wind speed (WS) 10 m above the sea level. An empirical modification based on that published in [50] is adopted here to ensure the model better fits L-band GNSS-R signals. It should be noted that both this model and its empirical modifications were determined using aircraft based receivers, being employed to directly detect oil-slicks under general scenarios. The MSS of a particular area is determined by the WS and the presence of oil. Hence, oil slicks on the ocean surface will affect the scattering coefficient distribution and thus change the corresponding DDM.

The reflection coefficient of the layered medium for microwave signals is analyzed in [46] where a 1-mm thick oil layer (typical value in real situations) is considered. The result shows that for signals such as these in the L1 band whose wavelengths (19 cm) are much larger than the oil thickness, the effect of oil on the reflection coefficient is negligible in most cases. However, when the grazing angle is between 0° and 20°, a pseudo-Brewster phenomenon arises which results in significant differences in the reflection coefficients of oil contaminated and clean sea surfaces. Under these circumstances, the corresponding scattering coefficients of oil slicked sea surfaces become much smaller, even smaller than the scattering coefficient of clean surface when the grazing angle is around 6° [46]. This would make it difficult to conduct oil spill detection. However, for GNSS-R based remote sensing, grazing angles are generally larger than 45°. For examples, for the UK-DMC satellite, the antenna 3 dB footprint is approximately 28° along-track and 70° cross-track [17]. To ensure a sufficient antenna gain, the grazing angle should not be smaller than 76° along-track and 55° cross-track. Hence, the pseudo-Brewster phenomenon will not affect the GNSS-R oil

slick detection in this satellite configuration, and, using the models described above, the DDMs over oil-slicked surfaces under general scenarios can be simulated.

2.2.3.4 Mapping Received Power to the DD Domain

Before calculating received power, the Σ of each grid element in the spatial domain can be obtained using

$$\Sigma(\vec{\rho}) = \frac{T_i^2 D^2(\vec{\rho})\sigma^0(\vec{\rho})ds}{4\pi R_R^2(\vec{\rho})R_T^2(\vec{\rho})} \tag{2.20}$$

where ds is the area of each grid element. Using the relationship between the spatial domain and DD domain, the Σ function can be mapped into the DD domain. Hence, $\Sigma(\Delta f, \Delta\tau)$ can be acquired.

The expression for the DDM in Eq. (2.1) can be rewritten as [39]

$$\left\langle |Y(\Delta\tau, \Delta f)|^2 \right\rangle = \chi^2(\Delta\tau, \Delta f) * \Sigma(\Delta\tau, \Delta f) \tag{2.21}$$

where "$*$" indicates a two dimensional convolution and $\chi(\Delta\tau, \Delta f) \approx \Lambda(\Delta\tau)S(\Delta f)$ is the Woodward ambiguity function (WAF) [42]. By taking advantage of the properties of the Fourier transformation ($\mathscr{F}[\cdot]$), Eq. (2.21) becomes [34]

$$\mathscr{F}[\left\langle |Y(\Delta\tau, \Delta f)|^2 \right\rangle] = \mathscr{F}[\Sigma(\Delta\tau, \Delta f)] \cdot \mathscr{F}[\chi^2(\Delta\tau, \Delta f)]. \tag{2.22}$$

Therefore, rather than conducting the convolution of WAF and Σ, multiplication of the Fourier transformations could be used to save time [39]. Then, by conducting the inverse Fourier transformation, the DDM $\langle |Y(\Delta\tau, \Delta f)|^2 \rangle$ will be acquired.

Figure 2.6: Gulf of Mexico, April 25, 2010. The "×" mark indicates the location of Station 42040 of National Data Buoy Center.

2.3 Results

The scattering coefficient distribution is modelled based on an oil spill which occurred in Gulf of Mexico in 2010. Fig. 2.6 shows the Moderate Resolution Imaging Spectroradiometer (MODIS) image of the extent of the oil spill on April 25 [51]. A uniformly distributed 6.8 m/s daytime WS, obtained from Station 42040 of National Data Buoy Center [52] shown in Fig. 2.6, is taken into account. In the simulation result for σ^0 in Fig. 2.7, the oil slicked area can be clearly distinguished. It should be noted that the scattering coefficient of the oil slick, compared with that of the clean ocean surface, decreases more rapidly when the scattering point moves away from the SP, because diffuse reflection becomes stronger and occurs more frequently for clean surfaces than for oil contaminated areas. Although the glistening zone could be more than 400 km in diameter [39], the area of the oil slick should be determined by the region where the scattering coefficients of oil slick are distinguishable. Fig. 2.8(a) shows the scattering coefficients of both the oil slicked area and the clean ocean surface when the WS is 6.8 m/s. Fig. 2.8(b) shows the ratio of the scattering coefficients for the two

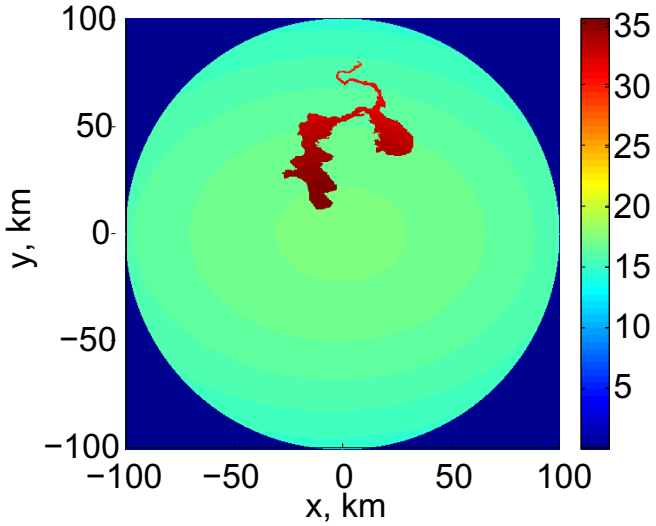

Figure 2.7: Simulated scattering coefficient distribution.

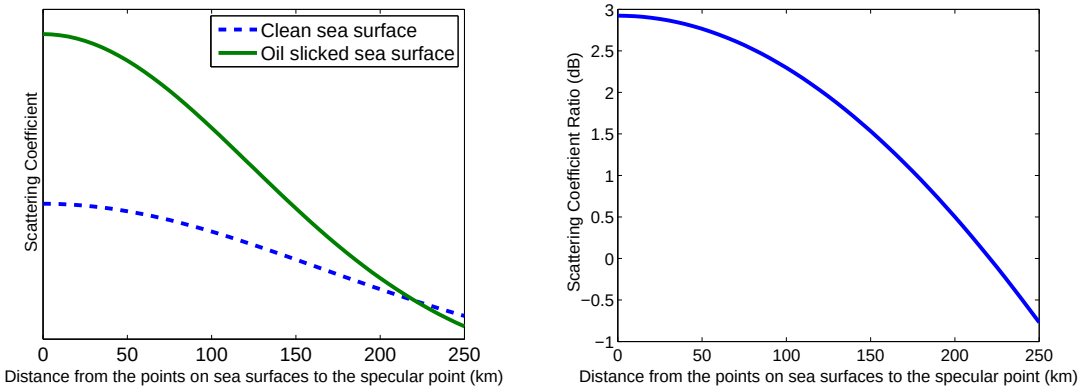

(a) (b)

Figure 2.8: (a) Scattering coefficients of oil contaminated areas and clean areas versus distance to the specular point. (b) The ratio between the scattering coefficients of oil slick and clean sea surfaces.

types of surface. As can be observed in these figures, the scattering coefficients of the two types of surfaces become identical at scattering points 220 km away from the SP, which suggests that the oil slick could be detected within this range limit. However, in order to achieve a large contrast between oil contaminated and clean surfaces so that the detection result will not be severely affected by noise, the radius of the detection area would have to be further reduced (120 km for 2 dB contrast and 80 km for 2.5

Table 2.1: General and Simplified Scenarios

	General Scenario	Simplified Scenario
Transmitter Position (10^6 m)	0, 0, 26682	0, 0, 26682
Transmitter Velocity (m/s)	0, -3000, 0	0, -3000, 0
Receiver Position (10^6 m)	1286, 1345, 6800	0, 0, 7050
Receiver Velocity (m/s)	6240, 4680, 0	0, 7800, 0
Elevation angle at SP	72.3°	90°(nadir reflection)
Coherent integration times	10ms	10ms

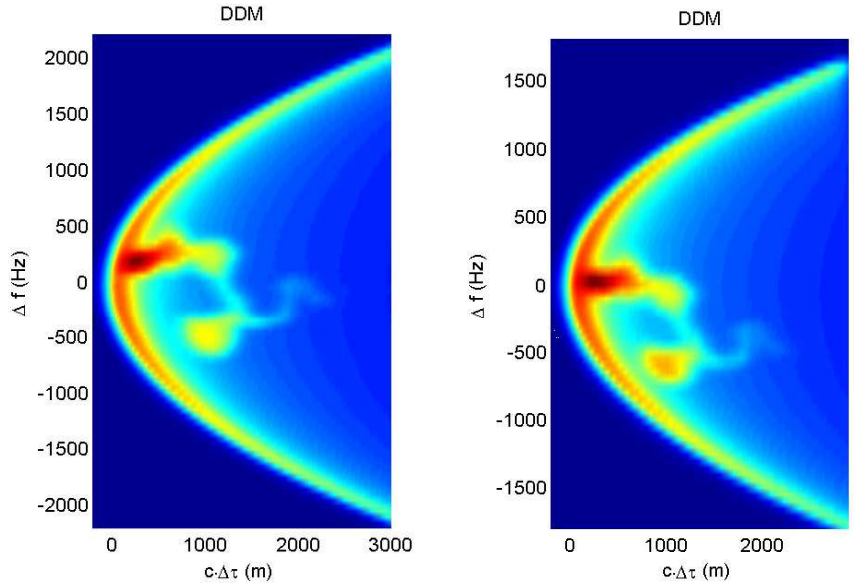

(a) (b)

Figure 2.9: Simulated DDM: (a) Simplified scenario; (b) General scenario.

dB contrast, according to Fig. 2.8(b)).

Both a simplified scenario and a general scenario are employed to generate DDMs based on Fig. 2.7. The simplified scenario is similar to the one applied by Valencia in [36], and the general scenario is the same as the simplified scenario except for the location and velocity of the receiver. A more specific description of the scenarios is shown in Table 2.1. The coherent integration time employed here is 10 ms, which is in accordance with [36]. The corresponding simulation results are shown in Fig. 2.9. As can be observed from the result, the simulated DDMs of the two scenarios are

different especially in the oil slicked area. The shape of the oil spill in the general scenario is slightly "twisted", because the variation in the orbiting direction of the transmitter and receiver may alter the contours of the iso-Doppler-frequency, so that the oil spill distribution in the DD domain is rearranged.

As mentioned previously, the application of the general scenario is broader than that of the simplified scenario. The passive GNSS-R receiver is more likely to detect the oil slick on the sea surface under the general scenario. Moreover, for a GNSS-R system with the antenna beam steered away from nadir by a small angle, e.g., the one used on the UK-DMC satellite [17], the DDM with the highest SNR could be obtained only under the general scenario with the elevation angle set accordingly to the antenna steering angle.

2.4 General Chapter Summary

This chapter discusses the DDM simulation process for an oil slicked area under a general scenario. An analysis of the received power from oil contaminated and clean sea surfaces indicates the radius of the oil slick detection area is about 100 km. In the simulation result, the difference between the two scenarios due to the general scenario can be observed clearly. In the next chapter, the simulated oil-slicked sea surface DDM under general scenarios is applied for an oil slick detection approach development.

Chapter 3

Oil-Spill Detection under General Reflection Geometries Using GNSS-R Delay Doppler Maps from Two Antennas

In the previous chapter, an algorithm to simulate ocean surface oil slick DDMs under general scenarios is presented. In this chapter, this result will be applied to develop an unique approach to detect sea surface oil spills. In Section 3.1, the basics of oil slick detection is discussed. In Section 3.2, the methodologies of improving detection accuracy and eliminating DDM ambiguity are described. Section 3.3 presents a means of characterizing the performance of the proposed oil-slick detection technique in terms of scattering coefficient retrieval accuracy and resolution. In Section 3.4, the performance of the proposed oil slick detection scheme is evaluated based on simulation. Section 3.5 presents a validation of this technique as applied to a real data set collected over land by the UK-DMC satellite. Finally, a summary is presented in

Section 3.6.

3.1 Basics of Oil Slick Detection Using GNSS-R

The effectiveness of oil spill detection depends on how well the signal wavelength and the damped surface surf wavelength match each other. It has been known for a long time that oil slicks on ocean surfaces dampen capillary waves [49]. The oil on the surface will also dampen waves less than 30 cm [33]. Hence, with a wavelength of 19 cm, L1 signals used by GNSS-R are capable of detecting these damped waves. This conclusion coincides with the result of the experiment described in [53], in which the L band signal provides a distinguishable contrast ratio (i.e., the ratio between the scattering coefficients of slick-covered and slick-free surfaces) of approximately 3 dB. It should be noted that L band signals may not be the best for oil slick discrimination, since X and C bands signals showed a 2.5 dB higher contrast ratio in the same experiment [53]. However, L-band is known to be sensitive to oil-induced changes of surface wave slopes, and we believe the potential advantages in temporal and spatial coverage offset these losses in sensitivity.

Along similar lines, the surface observables in a single SAR image are generally better than what can be achieved using GNSS-R. However, one needs to consider that the advantage of GNSS are primarily the improved coverage using a relatively cheap and simple instrument, capable of being launched in small constellations, such as NASA's CYGNSS mission [54]. Additionally, L band signals are suspected to be less sensitive (i.e., show lower contrast ratio) to some oil slick look-alikes than X and C bands, especially on certain types of biogenic films [55] which are relatively difficult to be distinguished from oil spills. Therefore, oil slick detection using GNSS-R can complement well the detection results from SAR or other sensing techniques that

observe different areas or operate at different frequencies.

Oil slick detection using GNSS-R is based on distinguishing the scattering coefficients of the sea surface, with and without an oil slick, from the DDMs using the scattering model in Eq. (2.1). By considering the effect of noise N, the DDM expression described in Eq. (2.1) can be rewritten as [39]

$$\left\langle |Y(\Delta\tau, \Delta f)|^2 \right\rangle = \chi^2(\Delta\tau, \Delta f) * \Sigma(\Delta\tau, \Delta f) + N \quad , \tag{3.1}$$

and Σ in Eq. (2.20) is defined as [39]

$$\Sigma(\Delta\tau, \Delta f) = T_i^2 \iint_A \frac{D^2(\vec{\rho})\sigma^0(\vec{\rho})}{4\pi R_R^2(\vec{\rho}) R_T^2(\vec{\rho})} \delta(\Delta\tau)\delta(\Delta f) d^2\rho. \tag{3.2}$$

where $\delta(\Delta\tau)$ and $\delta(\Delta f)$ are the Dirac delta functions of $\Delta\tau$ and Δf, respectively. In order to retrieve the scattering coefficient $\sigma^0(\vec{\rho})$, Σ needs to be determined from Eq. (3.1).

3.2 Oil Slick Detection Modelling

Due to the presence of noise in real applications, distortions will be induced when determining Σ. Thus, a method for correcting the corresponding distortions is proposed.

3.2.1 A Method for Correcting Distortions Due to CLS Filter

In order to retrieve the scattering coefficient distribution, the retrieval algorithm employs a constrained least squares (CLS) filter to "deblur" the DDMs, Y, and uses the

second order Laplacian operator p to deal with noise [34]

$$\mathscr{F}[\Sigma_\gamma(\Delta\tau,\Delta f)] = \frac{\mathscr{F}[\chi^2]^*}{|\mathscr{F}[\chi^2]|^2+\gamma|\mathscr{F}[p]|^2}\mathscr{F}[\left\langle|Y(\Delta\tau,\Delta f)|^2\right\rangle] \tag{3.3}$$

where $\mathscr{F}$ indicates the Fourier transformation operator, the superscript "*" indicates the complex conjugate operator, Σ_γ is the retrieved result of the deblurred DDM; γ is the weight parameter adjusted according to the SNR of the DDMs [56] and controls the trade-off between the smoothing effect and the restored detail of the scattering coefficient distribution.

For the sake of simplicity, Y and Σ denote, respectively, $Y(\Delta\tau,\Delta f)$ and $\Sigma(\Delta\tau,\Delta f)$ during the formula derivation process in this section. By substituting Eq. (3.1) into Eq. (3.3) we get

$$\mathscr{F}[\Sigma] + \frac{\mathscr{F}[N]}{\mathscr{F}[\chi^2]} = \frac{|\mathscr{F}[\chi^2]|^2+\gamma|\mathscr{F}[p]|^2}{|\mathscr{F}[\chi^2]|^2}\mathscr{F}[\Sigma_\gamma] \quad . \tag{3.4}$$

Using inverse Fourier transformation, the expression for Σ in terms of the retrieved Σ_γ can be determined from Eq. (3.4) as

$$\Sigma = \Sigma_\gamma + \Sigma_\gamma * \mathscr{F}^{-1}\left[\frac{\gamma|\mathscr{F}[p]|^2}{|\mathscr{F}[\chi^2]|^2}\right] - \mathscr{F}^{-1}\left[\frac{\mathscr{F}[N]}{\mathscr{F}[\chi^2]}\right] \tag{3.5}$$

By executing the expression $\Sigma - \Sigma_\gamma$, two distortion terms between the real Σ and the retrieved Σ_γ can be found. The term $\mathscr{F}^{-1}\left[\frac{\mathscr{F}[N]}{\mathscr{F}[\chi^2]}\right]$ is dependent of the noise itself, whereas the term $\Sigma_\gamma * \mathscr{F}^{-1}\left[\frac{\gamma|\mathscr{F}[p]|^2}{|\mathscr{F}[\chi^2]|^2}\right]$ is dependent on the CLS filter, which in turn is influenced by γ. In order to reduce the retrieval inaccuracy caused by the CLS filter a distortion correction is proposed here. To reduce the distortion for a specific $\Sigma_{1\gamma}$ retrieved from a DDM of an unknown surface, a distortion distribution $H_{0\gamma}$ is determined first by a simulation that assumes the observed surface is clean. Then,

the obtained $H_{0\gamma}$ can be applied to $\Sigma_{1\gamma}$ for distortion correction. More specifically, the simulated distortion distribution $H_{0\gamma}$ is calculated, without considering the noise, according to

$$H_{0\gamma} = \frac{\Sigma_0}{\Sigma_{0\gamma}} = I + \frac{\Sigma_{0\gamma} * \mathscr{F}^{-1}\left[\frac{\gamma|\mathscr{F}[p]|^2}{|\mathscr{F}[\chi^2]|^2}\right]}{\Sigma_{0\gamma}} \tag{3.6}$$

where Σ_0 is the real deblurred DDM of a clean surface and $\Sigma_{0\gamma}$ is the retrieved deblurred DDM of the clean surface using the CLS filter. It should be noted that the location information of the transmitter and receiver associated with $\Sigma_{1\gamma}$ needs to be employed while determining $H_{0\gamma}$. Then, the distortion distribution $H_{0\gamma}$ is used here to obtain the refined retrieved result, $\Sigma'_{1\gamma}$, from the uncorrected $\Sigma_{1\gamma}$ via

$$\Sigma'_{1\gamma} = \Sigma_{1\gamma} H_{0\gamma} = \Sigma_{1\gamma} + \frac{\Sigma_{1\gamma}}{\Sigma_{0\gamma}} \Sigma_{0\gamma} * \mathscr{F}^{-1}\left[\frac{\gamma|\mathscr{F}[p]|^2}{|\mathscr{F}[\chi^2]|^2}\right] \tag{3.7}$$

From Eq. (3.5), the real deblurred DDM can be expressed as

$$\Sigma_{1\gamma} = \Sigma_{1\gamma} + \Sigma_{1\gamma} * \mathscr{F}^{-1}\left[\frac{\gamma|\mathscr{F}[p]|^2}{|\mathscr{F}[\chi^2]|^2}\right] - \mathscr{F}^{-1}\left[\frac{\mathscr{F}[N]}{\mathscr{F}[\chi^2]}\right] \tag{3.8}$$

The difference between the refined result and the real deblurred DDM can then be expressed as

$$\begin{aligned} \Sigma_1 - \Sigma'_{1\gamma} = &- \frac{\Sigma_{1\gamma}}{\Sigma_{0\gamma}} \left(\Sigma_{0\gamma} * \mathscr{F}^{-1}\left[\frac{\gamma|\mathscr{F}[p]|^2}{|\mathscr{F}[\chi^2]|^2}\right]\right) \\ &+ \Sigma_{1\gamma} * \mathscr{F}^{-1}\left[\frac{\gamma|\mathscr{F}[p]|^2}{|\mathscr{F}[\chi^2]|^2}\right] - \mathscr{F}^{-1}\left[\frac{\mathscr{F}[N]}{\mathscr{F}[\chi^2]}\right] \end{aligned} \tag{3.9}$$

It can be observed from Eq. (3.9) that the noise distortion term $\mathscr{F}^{-1}\left[\frac{\mathscr{F}[N]}{\mathscr{F}[\chi^2]}\right]$ is the

same as that of $\Sigma_{1\gamma}$, whereas its CLS distortion term,

$$-\frac{\Sigma_{1\gamma}}{\Sigma_{0\gamma}}\left(\Sigma_{0\gamma} * \mathscr{F}^{-1}\left[\frac{\gamma|\mathscr{F}[p]|^2}{|\mathscr{F}[\chi^2]|^2}\right]\right) + \Sigma_{1\gamma} * \mathscr{F}^{-1}\left[\frac{\gamma|\mathscr{F}[p]|^2}{|\mathscr{F}[\chi^2]|^2}\right] \quad , \tag{3.10}$$

is affected by the degree of similarity between the distortion distributions of different surface states. More specifically, if the distortion distributions of different surface states are the same, i.e. $H_{0\gamma} = H_{1\gamma}$, Eq. (3.7) becomes

$$\Sigma'_{1\gamma} = \Sigma_{1\gamma}H_{1\gamma} = \Sigma_{1\gamma} + \Sigma_{1\gamma} * \mathscr{F}^{-1}\left[\frac{\gamma|\mathscr{F}[p]|^2}{|\mathscr{F}[\chi^2]|^2}\right] \tag{3.11}$$

In this case, the CLS distortion term in Eq.(3.9) will become zero. On the other hand, if there is a significant difference between the distributions of different surfaces, the CLS distortion term in Eq.(3.9) can be larger than that of $\Sigma_{1\gamma}$. To better exploit the similarity between different distortion distributions, the value of H_γ is compared for sea surfaces under different states. Fig. 3.1(a), Fig. 3.1(b) and Fig. 3.1(c) indicate the scattering coefficient distributions of a clean surface, a fully oil-contaminated surface and a partially contaminated surface, respectively. Their corresponding distortion distributions are shown, respectively, in Fig. 3.1(d), Fig. 3.1(e) and Fig. 3.1(f). A simple rectangular-shaped oil slick is used for the partially contaminated surface in Fig. 3.1(c) to highlight the difference between oil-covered and oil-free areas. This research employs an assumption of a uniformly distributed surface wind. The value of γ used here is 32. This value corresponds to the SNR of the 1 s incoherent integration result shown in Fig. 3.4(b). A more specific methodology to determine γ for different signals is discussed in Section 3.3.1. From Fig. 3.1, it can be observed that the distortion distribution of the clean surface resembles precisely that of the fully contaminated surface. This correlates well with Eq. (3.9) by letting $\Sigma_{1\gamma} = c\Sigma_{0\gamma}$ where c indicates the ratio between the scattering coefficient of oil-covered and oil-free

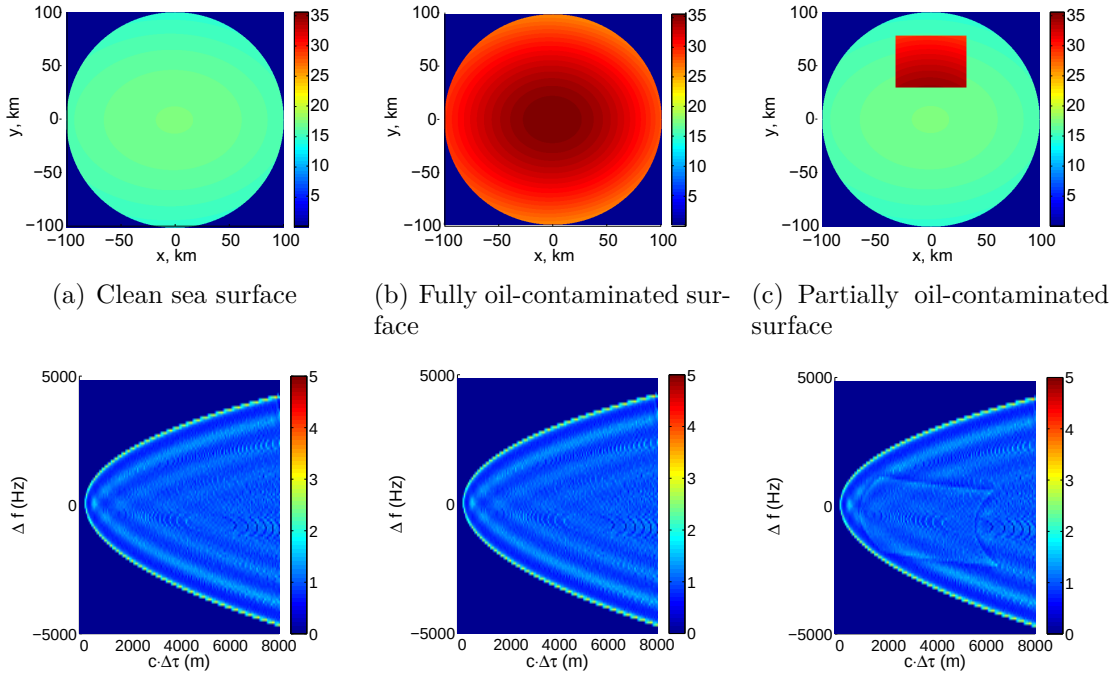

(a) Clean sea surface

(b) Fully oil-contaminated surface

(c) Partially oil-contaminated surface

(d) Clean sea surface.

(e) Fully oil-contaminated surface.

(f) Partially oil-contaminated surface.

Figure 3.1: Scattering coefficient distribution σ^0 and distortion distribution H_γ ($\gamma = 32$) for different sea surface states.

surfaces. By employing the reflection coefficient model and mean-square slope model for both oil-covered and oil-free surfaces discussed in Chapter 2, a ratio of 3.2 dB is obtained. This agrees well with the experimental result of the L-band signal obtained in [53]. When comparing Fig. 3.1(f) to Fig. 3.1(d), close similarities can be found between these distortion distributions from a general perspective. A closer inspection shows that the differences of Fig. 3.1(f) with respect to Fig. 3.1(d) increase up to 32% at the oil slick boundary and reduce to less than 5% when moving towards the oil slick centre. This suggests that although the retrieval inaccuracy may increase at the oil boundary, most of the distortions induced by the CLS filter can be effectively reduced using the method proposed in this chapter. It is important to note that the CLS filter in Eq. (3.3) is a classical image restoration method which is well developed and capable of dealing with various degraded images. The reason why the adjustment suggested in Eq. (3.7) can be applied here is because of the similarity of the distortion distribution under various surface conditions. Thus, this adjustment is not a general distortion correction algorithm for CLS restored images. Rather, it can only be used here for GNSS-R ocean surface sensing.

After distortion correction, the resultant Σ'_γ can be used to retrieve the scattering coefficient. The previous simulated detection [36] uses the Jacobian approach for this analysis. Here, a full surface spatial integration is employed to retrieve $\sigma^0(\vec{\rho})$.

3.2.2 Spatial Integration Approach

Unlike the Jacobian approach which uses the mathematical relationship between the spatial and delay-Doppler (DD) domain to generate the Jacobian matrix [39], the spatial integration approach (SIA) uses the integration in Eq. (3.2) directly to obtain Σ. During the process of mapping scattering coefficients from the DD domain to the spatial domain, each DD point corresponds to two spatial positions due to a mapping

ambiguity. For space-based GNSS-R receivers, an assumption will usually be made that the points in the spatial domain are denser than those in the DD domain, i.e., there are more spatial points than DD points for the same sea surface area. Therefore, each DD point actually corresponds to two clusters of spatial points as shown in Fig. 2.2, page 14.

In previous work, to solve the ambiguity problem, spatial filtering was applied to the simulated DDM by tilting the antenna beam away from the ambiguity free line [36]. In order for this spatial filtering to work, only the DDM on one side of the ambiguity line can be used. This technique is summarized below to better frame the problem. We will then propose a solution using two antenna beams, as discussed in Section 3.2.5.

When using a spatial filter, each DD point will correspond to several spatial points in two areas symmetric around the center line. Consider the DD point $(\Delta\tau_0, \Delta f_0)$ as an example:

$$(\Delta\tau_0, \Delta f_0) \leftrightarrow \begin{cases} \vec{\rho}_0 = (x_0, y_0) \\ \vec{\rho}_1 = (x_1, y_1) \\ \qquad\qquad . \\ \qquad\qquad . \\ \vec{\rho}_n = (x_n, y_n) \end{cases} \tag{3.12}$$

where the spatial points $\vec{\rho}_0$ to $\vec{\rho}_n$ correspond to the same DD point $(\Delta\tau_0, \Delta f_0)$. As can be seen in Fig. 2.2, when mapping the scattering coefficient distribution retrieved from the DD domain to that in the spatial domain, the scattering coefficients of both clusters of spatial points corresponds to one DD point. It is not possible to distinguish the difference in scattering coefficients of the spatial points in these two clusters. Thus, an assumption is made in the SIA as well as in the Jacobian approach [34] that the σ^0 is uniformly distributed within this total spatial area (i.e. the two clusters of

spatial points). This permits σ^0 moving outside the integral in Eq. (3.2), allowing the equation to be rewritten as

$$\begin{aligned}\Sigma(\Delta\tau,\Delta f) &= T_i^2\sigma^0(\Delta\tau,\Delta f)\\ &\times \iint_A \frac{D^2(\vec{\rho})}{4\pi R_R^2(\vec{\rho})R_T^2(\vec{\rho})}\delta(\Delta\tau)\delta(\Delta f)d^2\rho\end{aligned} \tag{3.13}$$

Hence, σ^0 in the DD domain can be acquired by using the expression

$$\begin{aligned}\sigma^0(\Delta\tau,\Delta f) &= \frac{4\pi\Sigma(\Delta\tau,\Delta f)}{T_i^2}\\ &\times \frac{1}{\iint_A \frac{D^2(\vec{\rho})}{R_R^2(\vec{\rho})R_T^2(\vec{\rho})}\delta(\Delta\tau)\delta(\Delta f)d^2\rho}\end{aligned} \tag{3.14}$$

It should be noted that for each $\sigma^0(\Delta\tau,\Delta f)$ in Eq. (3.14), the Dirac delta functions $\delta(\Delta\tau)$ and $\delta(\Delta f)$ delimit the integral range from the entire glistening zone A to the spatial points that correspond only to $(\Delta\tau,\Delta f)$. Thus, the scattering coefficient of each DD bin is determined by the averaged spatial characteristics within the total contributing area. By conducting the spatial integration over the entire glistening zone A, the scattering coefficient distribution in the entire DD domain is obtained.

Finally, as demonstrated in [41], in order for each DD point to be uniquely associated with a single area on the surface, only half of the glistening zone is used to generate the DDM. In this case the scattering coefficient distribution can be mapped directly into the spatial domain [47, 48]. In the case where one side of the ambiguity line can't be eliminated using the satellite antenna, and scattered power from the two distinct regions freely mixes, a new technique is needed. We will show that by viewing the oil slick region using two separate antennas from different viewing angles, the contribution from each of the separate patches can be estimated and an unambiguous surface map produced. The technique, which requires several extra steps to determine

the spatial distribution of σ^0 on the surface, is described in Section 3.2.5.

3.2.3 Comparison of Spatial Integration and Jacobian Approaches

In this subsection, the Jacobian approach and the SIA are compared to assess their respective accuracies. The difference between the Jacobian approach and the SIA for obtaining the scattering coefficient lies mainly in the calculation of the double integral of Σ in Eq. (3.2). The Jacobian approach uses the mathematical relationship between the spatial and DD domains to change the variables [39]:

$$\begin{aligned}&\Sigma(\Delta\tau, \Delta f) = \\ &\frac{D^2(\vec{\rho}(\Delta\tau, \Delta f))\sigma^0(\vec{\rho}(\Delta\tau, \Delta f))}{4\pi R_R^2(\vec{\rho}(\Delta\tau, \Delta f))R_T^2(\vec{\rho}(\Delta\tau, \Delta f))} T_i^2 \left|J(\Delta\tau, \Delta f)\right|\end{aligned} \tag{3.15}$$

By applying the aforementioned assumption that scattering coefficient σ^0 is uniformly distributed throughout each spatial cluster, σ^0 could be obtained by rewriting Eq. (3.15):

$$\begin{aligned}\sigma^0(\Delta\tau,\Delta f) = &\frac{4\pi\Sigma(\Delta\tau, \Delta f)}{T_i^2} \\ &\times \frac{R_R^2(\vec{\rho}(\Delta\tau, \Delta f))R_T^2(\vec{\rho}(\Delta\tau, \Delta f))}{D^2(\vec{\rho}(\Delta\tau, \Delta f))\left|J(\Delta\tau, \Delta f)\right|}\end{aligned} \tag{3.16}$$

where $|J|$ indicates the determinant of the Jacobian matrix, i.e.,

$$\left|J(\Delta\tau, \Delta f)\right| = \det \begin{vmatrix} \frac{\partial x}{\partial(\Delta\tau)} & \frac{\partial x}{\partial(\Delta f)} \\ \frac{\partial y}{\partial(\Delta\tau)} & \frac{\partial y}{\partial(\Delta f)} \end{vmatrix} . \tag{3.17}$$

In Eq. (3.17), x and y represent the coordinates of a spatial point $\vec{\rho}$ that corresponds to the DD coordinate $(\Delta\tau, \Delta f)$. Despite the fact that $(\Delta\tau, \Delta f)$ actually corresponds to a cluster of spatial points, with several approximations employed by the algorithm

[39], only one spatial point, which is denoted as $\vec{\rho}(\Delta\tau, \Delta f)$ in Eq. (3.15), will be determined. With this point determined, the computation of the determinant of the Jacobian matrix can be accomplished by substituting the derivatives with their associated finite-difference approximations [39]; i.e.,

$$\begin{aligned} \frac{\partial x}{\partial(\Delta\tau)} &\approx \frac{x(\Delta\tau + \tau_\delta/2, \Delta f) - x(\Delta\tau - \tau_\delta/2, \Delta f)}{\tau_\delta} \\ \frac{\partial x}{\partial(\Delta f)} &\approx \frac{x(\Delta\tau, \Delta f + f_\delta/2) - x(\Delta\tau, \Delta f - f_\delta/2)}{f_\delta} \end{aligned} \tag{3.18}$$

where τ_δ and f_δ indicate the delay and Doppler resolution, respectively. The derivatives of y can be obtained in a similar way.

In addition to the approximations applied in the determination of the Jacobian matrices, another approximation is also employed. To make the approximation easier to understand, the DD point $(\Delta\tau_0, \Delta f_0)$ in Eq. (3.12) is taken as an example: in order to determine $\Sigma(\Delta\tau_0, \Delta f_0)$, the spatial integration in Eq. (3.2) with integration limits from $\vec{\rho}_0$ to $\vec{\rho}_n$ is assumed to be equivalent to the multiplication of the spatial point $\vec{\rho}(\Delta\tau, \Delta f)$ and the Jacobian determinant $|J(\Delta\tau, \Delta f)|$. Although these approximations help in reducing the computational cost of the Jacobian approach, corresponding errors will occur in the retrieval process. Since the SIA does not impose these assumptions, more accurate results can be obtained.

3.2.4 General Scenario

The oil slick detection algorithm that deals only with the simplified scenario is obviously insufficient to apply to an operational satellite mission. The approach that extends the DDM simulation procedure to general scenarios was first proposed in [47]. In the retrieval process, additional modifications are needed. Notably, the scenario geometry and receiver configuration need to be carefully adjusted to match those of

the measured DDM.

As can be seen from Eq. (3.14), in order to retrieve scattering coefficients, the algorithm must be capable of determining the Doppler shift and signal delay of surface points under general scenarios. The geometry and dynamics of the remote sensing system during data collection is known to a reasonably high degree of accuracy, being provided by the satellite GPS navigation unit and data from the International GNSS Service (IGS). Then, the position of the SP, around which a map of relative delays, $\Delta\tau$, and Dopplers, Δf, can be generated, is determined. The SP can be calculated using, for example, the methods presented in [7, 47]. Subsequently, the locations and velocities of the transmitter and receiver are transformed into the ECXI coordinate system [47] to simplify the calculation of the Doppler shift and C/A delay for each surface point.

It should be noted that in the scattering coefficient determination process, the parameters related to data collection and receiver configuration must be well known in order to accurately connect the physical scattering surface to individual points in the DDM. In particular, this includes a detailed knowledge of the antenna pattern and steering angle during data collection. The differences in the DDMs from these two antennas are key to resolving the surface ambiguity as described below.

3.2.5 Ambiguity Resolution

The ambiguity problem refers to the fact that reflected power from two distinct (and often vastly separate) physical regions on the ocean surface contribute to the power of a single DD bin. Since the contours of iso-delay, as shown in Fig. 2.2, are concentric ellipses, every point in the DD domain corresponds to two positions in the spatial domain. In other words, each DD bin is the accumulation of power from two clusters of spatial regions.

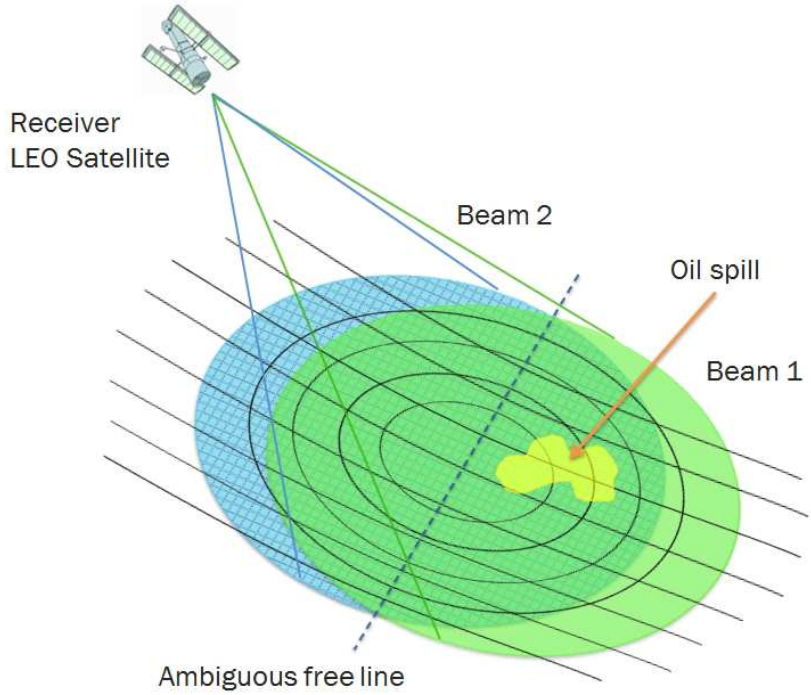

Figure 3.2: Adopting two antenna beams to avoid ambiguity.

Due to the ambiguity property of the DDMs, for each DD point $\Sigma(\Delta\tau, \Delta f)$, it is difficult to determine the proportion of power contributed by each of the two spatial clusters. To achieve an effective spatial filtering at satellite altitudes, the contribution from one ambiguity-free zone would need to be at least an order of magnitude lower than the other in order to achieve adequate isolation of the desired half of the glistening zone. Although may be possible, correctly orienting an antenna beam with such a sharp cut-off would be challenging. The antenna would need to be steered accurately to isolate precisely only half of the glistening zone around the ambiguity line. An alternative would be to use two larger footprint antennas together and eliminate the need for active antenna beam steering. Therefore, in order to obtain a spatially unambiguous distribution of the scattering coefficients, two DDMs that come from two antenna beams can be used as shown in Fig. 3.2. In this figure, the area of interest is marked by the concentric circles. The ellipses with and without the grid

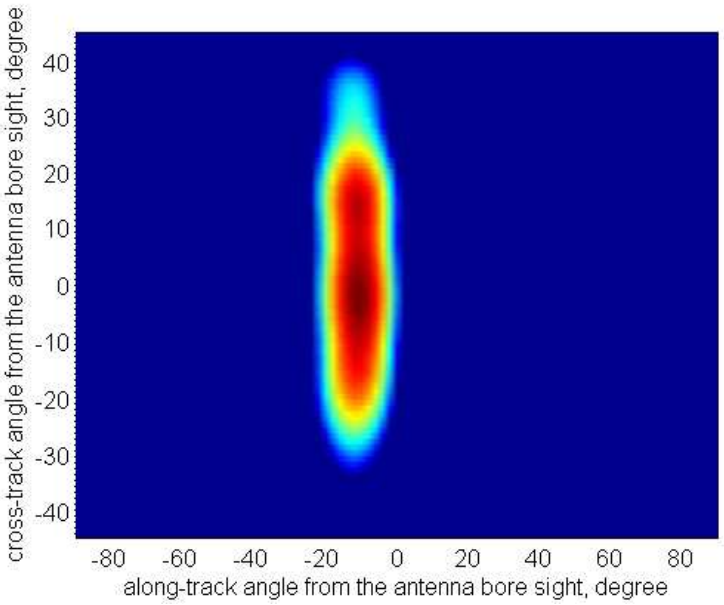

Figure 3.3: 3 dB ellipse of the UK-DMC antenna pattern.

represent the regions illuminated by the two antenna beams.

The antenna pattern and gain are set the same as those of the UK-DMC satellite as shown in Fig. 3.3. The two beams are tilted away from the SP in the two opposing directions perpendicular to the ambiguity free line, and the specular point is on the -3 dB contour of the antenna pattern. With two antenna beams, the ambiguity problem in scattering coefficient distribution retrieval can be solved using either the Jacobian approach or the SIA. This technique employs both approaches with the corresponding results compared and analyzed (see Section 3.4).

By applying the assumption that the scattering coefficients are uniformly distributed within each DD point, the expressions Σ_1 and Σ_2 from Eq. (3.2) can be

rewritten as:

$$\begin{aligned}
&\Sigma_1(\Delta\tau, \Delta f) = \\
&T_i^2 \sigma_1^0(\Delta\tau, \Delta f) \times \iint\limits_{A_1} \frac{D_1^2(\vec{\rho})}{4\pi R_R^2(\vec{\rho}) R_T^2(\vec{\rho})} \delta(\Delta\tau)\delta(\Delta f) d^2\rho \\
&+T_i^2 \sigma_2^0(\Delta\tau, \Delta f) \times \iint\limits_{A_2} \frac{D_1^2(\vec{\rho})}{4\pi R_R^2(\vec{\rho}) R_T^2(\vec{\rho})} \delta(\Delta\tau)\delta(\Delta f) d^2\rho
\end{aligned} \tag{3.19}$$

$$\begin{aligned}
&\Sigma_2(\tau, f_d) = \\
&T_i^2 \sigma_1^0(\Delta\tau, \Delta f) \times \iint\limits_{A_1} \frac{D_2^2(\vec{\rho})}{4\pi R_R^2(\vec{\rho}) R_T^2(\vec{\rho})} \delta(\Delta\tau)\delta(\Delta f) d^2\rho \\
&+T_i^2 \sigma_2^0(\Delta\tau, \Delta f) \times \iint\limits_{A_2} \frac{D_2^2(\vec{\rho})}{4\pi R_R^2(\vec{\rho}) R_T^2(\vec{\rho})} \delta(\Delta\tau)\delta(\Delta f) d^2\rho
\end{aligned} \tag{3.20}$$

where Σ_1 and Σ_2 are obtained from the two DDMs generated using the two antenna beams; D_1 and D_2 represent the pattern of the two beams; A_1 and A_2 are the two ambiguity-free zones symmetrical to each other; $\sigma_1^0(\Delta\tau, \Delta f)$ and $\sigma_2^0(\Delta\tau, \Delta f)$ are the scattering coefficients from area A_1 and area A_2, respectively. From the ambiguity problem, we know that $\sigma_1^0(\Delta\tau, \Delta f)$ and $\sigma_2^0(\Delta\tau, \Delta f)$ contribute to the same point $(\Delta\tau, \Delta f)$ in the DDMs, but their scattering coefficients could be different.

The antenna gain D, distance parameters R_R and R_T, relative Doppler shift Δf and C/A delay $\Delta\tau$ of every spatial point need to be determined in order to complete the integrations in Eq. (3.19) and Eq. (3.20). The detailed calculation process of these parameters can be found in [7, 47]. For the sake of simplicity, the integration $\iint\limits_{A_1} \frac{D_1^2(\vec{\rho})}{4\pi R_R^2(\vec{\rho}) R_T^2(\vec{\rho})} \delta(\Delta\tau)\delta(\Delta f) d^2\rho$ is referred to as $a_1(D_1, \Delta\tau, \Delta f)$ where the subscript 1 denotes the ambiguity-free zone A_1. Similarly, the other three integrations are referred to as $a_2(D_1, \Delta\tau, \Delta f), a_1(D_2, \Delta\tau, \Delta f)$ and $a_2(D_2, \Delta\tau, \Delta f)$, respectively. It is worthy of note that a_1 and a_2 as well as the coherent integration time T_i are all determined by the satellite locations and antenna gain. Following these considerations, scattering

coefficient σ^0, the only term affected by the sea surfaces, could be determined by rewriting Eq. (3.19) and Eq. (3.20):

$$\begin{aligned}\Sigma_1(\Delta\tau,\Delta f) &= T_i^2\sigma_1^0(\Delta\tau,\Delta f)a_1(D_1,\Delta\tau,\Delta f)\\ &\quad + T_i^2\sigma_2^0(\Delta\tau,\Delta f)a_2(D_1,\Delta\tau,\Delta f)\end{aligned} \tag{3.21}$$

$$\begin{aligned}\Sigma_2(\Delta\tau,\Delta f) &= T_i^2\sigma_1^0(\Delta\tau,\Delta f)a_1(D_2,\Delta\tau,\Delta f)\\ &\quad + T_i^2\sigma_2^0(\Delta\tau,\Delta f)a_2(D_2,\Delta\tau,\Delta f).\end{aligned} \tag{3.22}$$

By Knowing Σ_1, Σ_2, a_1, a_2 and T_i, the two unknowns σ_1^0 and σ_2^0 can be obtained by solving the two simultaneous equations Eq. (3.21) and Eq. (3.22). Once σ_1^0 and σ_2^0 are obtained in the DD domain, they can be mapped to the spatial domain without ambiguity.

3.3 Performance Characterization

To fully evaluate the performance of the proposed approaches, the retrieval inaccuracy and resolution are determined with respect to the SNR and the oil slick size.

3.3.1 Inaccuracy under Various SNR Levels

In addition to the inaccuracies induced through the process of deducing the scattering coefficient, a more important factor that contaminates the results is the presence of noise. Thus, the methodology of characterizing the inaccuracy under different SNR levels is described here.

In a real GNSS-R operational system, received signals are contaminated by both speckle noise and thermal noise. The speckle noise is due to the mixing of various carrier phases from different reflecting facets which results in a fluctuation in the

received signal as a function of time. Its effect can be mitigated if the received signals are averaged over consecutive coherent correlations. Generally, most of the speckle noise can be mitigated if the signal is averaged over 200 ms or more [17]. Since a 1000 ms incoherent integration is generally allowed for real-space application, the speckle noise should not have a large impact. Thus, only the thermal noise is considered in the simulation, and it is modelled as a Gaussian distribution.

Here, both the absolute SNR and the processed SNR are used to quantify the thermal noise. The absolute SNR (the ratio of mean signal power to mean noise power [57]) is very similar to the generally defined SNR, whereas the processed SNR reveals the variation of measured signal by indicating how much the signal exceeds the RMS noise floor [17]. When conducting oil slick detection from a measured signal, the magnitude of the retrieved scattering coefficient is affected by the absolute SNR, and the accuracy of the result is affected by the processed SNR_p. This can be expressed as [17]

$$\mathrm{SNR}_p = \frac{\langle |Y(\Delta\tau, \Delta f)|^2 \rangle - \overline{\langle |Y_N|^2 \rangle}}{RMS(\langle |Y_N|^2 \rangle - \overline{\langle |Y_N|^2 \rangle})} \tag{3.23}$$

where $\langle |Y_N|^2 \rangle$ is the noise power calculated from a region of the DDM where no signals are presented; and $\overline{\langle |Y_N|^2 \rangle}$ is the mean value of $\langle |Y_N|^2 \rangle$. As can be seen in Eq. (3.23), the SNR_p is inversely proportional to the noise standard deviation determined by the consecutive incoherent integration time [5]. Once the variance value of one correlation waveform is assigned, the SNR_p of the signal under different incoherent integration times can be determined. This is essential when simulating the signal with different SNR_p. In this chapter, the simulated noise variance of a single correlation result is set according to the PRN-28 dataset on March 12 [5] as shown in Fig. 3.4(a). This single correlation result corresponds to an incoherent integration interval of 1 ms. Using the inverse proportion between SNR_p and the standard deviation of the noise, the incoherent integration results of 1 s is shown in Fig. 3.4(b). This is the longest

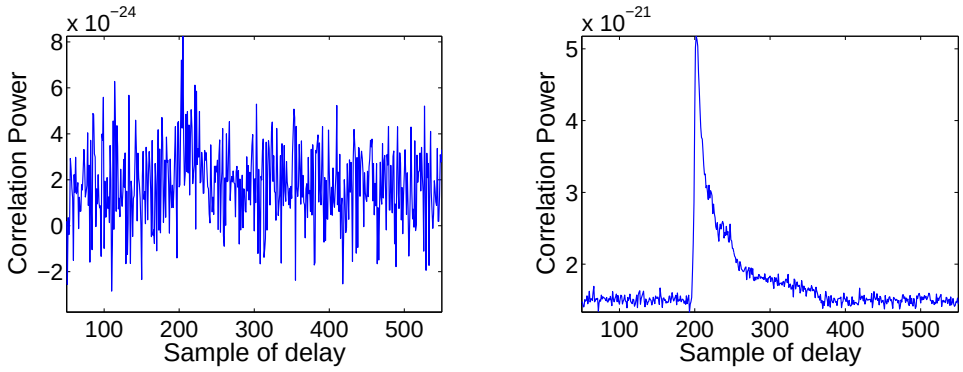

(a) (b)

Figure 3.4: Delay waveforms with incoherent integration interval of (a) 1 ms (b) 1 s.

interval during which the observation surface can be considered to be the same area for space-based receivers. From Eq. (3.23), the 1 ms and 1 s results correspond to an SNR_p of 6.5 dB and 18.5 dB, respectively.

A comparison between Fig. 3.4(a) and Fig. 3.4(b) indicates that the high noise variance present in the single correlation result can be easily decreased using incoherent integration. To investigate the performance of the SIA, the SNR_p range is set from 9.3 to 23.5 dB hereafter. This range corresponds to an incoherent integration interval of 10 ms to 10 s. Although the incoherent interval of 10 s is too long for a space-based receiver, the purpose of employing the corresponding SNR of 23.5 dB is to investigate the possible performance of the proposed technique when a better receiver configuration can be used.

For a specified SNR, the accuracy of the retrieval of $\Sigma_\gamma(\Delta\tau, \Delta f)$ in Eq. (3.3) depends on the weight parameter γ. If the γ is poorly set, Eq. (3.21) and Eq. (3.22) may be ill-posed and not have a unique solution. Thus, it is important to set an appropriate value for γ. In this chapter, the RMS of the difference between the retrieved Σ_γ and the real Σ is determined with respect to SNR_p for different γ as shown in Fig. 3.5(a). The γ corresponding to the smallest RMS value for a given SNR_p is considered to be the optimum value for that SNR_p. The optimum values are

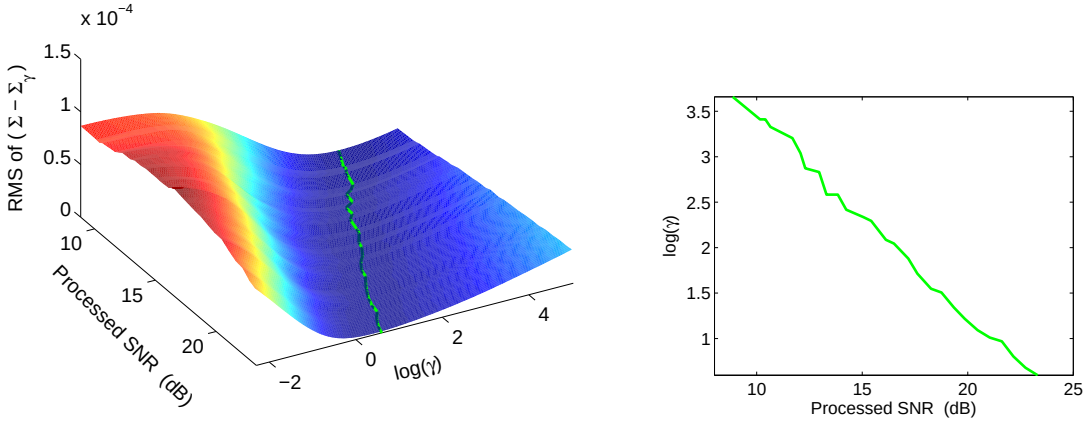

(a) (b)

Figure 3.5: (a) The RMS of the difference between the retrieved Σ_γ and the real Σ. (b) The optimal γ with respect to SNR_p.

indicated by the dashed line in Fig. 3.5(a) and in Fig. 3.5(b) where it is shown that the logarithm value of the weight parameter decreases almost linearly as the SNR_p value increases.

Once the corresponding γ is determined for given a measured DDM according to its SNR_p, the error of the retrieved σ^0 can be determined with respect to the original scattering coefficient. This relative error is calculated by

$$\alpha = \frac{|\sigma^\circ_\gamma - \sigma^\circ|}{\sigma^\circ} \tag{3.24}$$

where σ°_γ and σ° are the retrieved and original scattering coefficients, respectively.

3.3.2 Retrieval Spatial Resolution under Various SNR Levels

To investigate the resolution of the proposed oil slick detection technique, it is important to distinguish between the resolution of the original DDM, Y, and that of the de-blurred DDM, Σ_γ. It can be observed from Eq. (3.14) that the oil slick de-

tection resolution is identical to the de-blurred DDM resolution rather than to the original DDM resolution. With the presence of noise, the resolution of the retrieved de-blurred DDM Σ_γ varies with SNR_p. Thus, this technique uses a method to determine the retrieved de-blurred DDM resolution based on the resolution of the original DDMs.

It can be observed from Eq. (3.1) that Σ is blurred by the Woodward ambiguity function (WAF) χ^2, and thus the resolution of the original DDM is determined by the size of χ^2. By mapping the WAF from the DD domain into the spatial domain, the resolution of the original DDM can be obtained. The same concept has been used in the realm of bistatic SAR to determine spatial resolutions [58]. In the same way, the resolution of the de-blurred DDM is investigated by performing an inverse Fourier transformation on Eq. (3.4) to obtain the expression of the retrieved Σ_γ as

$$\begin{aligned}\Sigma_\gamma = &\mathscr{F}^{-1}\left\{\frac{|\mathscr{F}[\chi^2]|^2}{|\mathscr{F}[\chi^2]|^2+\gamma|\mathscr{F}[p]|^2}\right\} * \Sigma \\ &+ \mathscr{F}^{-1}\left\{\frac{\mathscr{F}[\chi^2]^*}{|\mathscr{F}[\chi^2]|^2+\gamma|\mathscr{F}[p]|^2}\right\} * N\end{aligned} \tag{3.25}$$

By comparing Eq. (3.1) with Eq. (3.25), it can be noted that the resolution of the retrieval result is determined by the extent size of the inverse-Fourier-transformation term

$$\mathscr{F}^{-1}\left\{\frac{|\mathscr{F}[\chi^2]|^2}{|\mathscr{F}[\chi^2]|^2+\gamma|\mathscr{F}[p]|^2}\right\} \tag{3.26}$$

which in turn is dependent on the weight parameter γ. For simplicity, this transformation term is hereafter referred to as the "resolution term". The resolution term is then projected from the DD domain into the spatial domain. The extent size in the spatial domain is considered to be the retrieval spatial resolution. More specifically, the extents of the resolution term along the delay (τ) and Doppler (f) axes in the DD domain correspond respectively to the resolutions along the radial and tangential

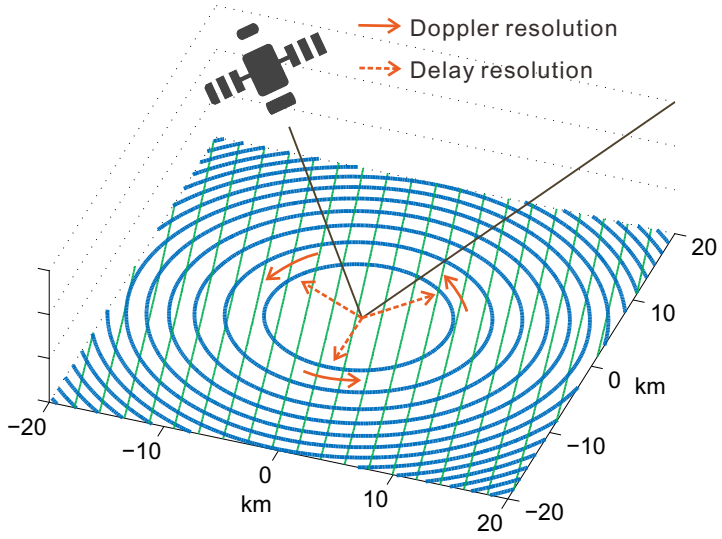

Figure 3.6: Spatial resolution: the delay resolution is indicated by the dashed arrow and the Doppler resolution is indicated by the solid arrow. The separation of iso-Doppler lines and iso-delay lines are 100 Hz and 0.179 chip (sampling rate = 5.714 MHz according to UK-DMC), respectively.

direction of a surface point relative to the SP, as shown in Fig. 3.6. The spatial resolutions determined by τ and f are hereafter referred to as the delay resolution, ΔR_τ, and the Doppler resolution, ΔR_f, respectively.

As previously mentioned, the processed SNR and the weight parameter are inversely correlated. In ideal cases without the presence of noise, γ would be 0. In this case, the resolution term becomes an impulse function with no extent, i.e., a single DD point. This suggests that without the presence of noise the retrieval resolution would only depend on the receiver sampling rate and Doppler shift bin. It should be noted that, the distortion distribution for a clean surface, $H_{0\gamma}$ proposed in this research changes the distortion of the CLS filter only and does not change the retrieval resolution. Hence, the resolution of the de-blurred DDM is the same as that of the de-blurred DDM after distortion correction. Also, it can be observed from Eq. (3.25) that the resolution of the de-blurred DDM is independent of the DDM magnitude

and, thus, independent of the absolute SNR.

3.3.3 Accuracy of Retrieved σ^0 under Various Oil Slick Sizes

In this work, it is observed that the dependence of the retrieval accuracy on noise varies with the oil spill size. In other words, under the same SNR_p condition, an oil slick with small size will appear less obvious in the retrieved scattering coefficient distribution. Considering this, the oil slick detection performance will be evaluated with respect to the oil slick size as well as the processed SNR. In this process, the oil slick shapes remain the same as the one shown in Fig. 2.7 but the sizes changed.

3.4 Simulation Results

The April 25, 2010 observation of the Deepwater Horizon oil spill demonstrated in Fig. 2.7 is used as an example to test the above algorithms. From Fig. 2.6, the oil slick is estimated to cover about 1000 km^2 ocean surface. Both simplified and general scenarios are considered in this simulation based on the parameters listed in Table 2.1. As discussed earlier in this chapter, the coherent integration time is set as 1 ms here. The simplified scenario is similar to that employed in [37]. The general scenario with a grazing angle of 76° is generated based on the reflection geometry of the GNSS-R ocean data provided in [44] collected by the UK-DMC satellite. Using the simulation procedure discussed in Chapter 2, the corresponding DDMs for the scenario are generated in Fig. 3.7.

In order to make the simulation of the DDMs more realistic, the simulated GNSS-R receiver configuration is set according to the DDMs measured by the UK-DMC satellite [5,17]. The Doppler frequency spacing of the DDM is calculated in increments of 100 Hz and the sampling rate of the simulated receiver is set at 5.714 MHz. As

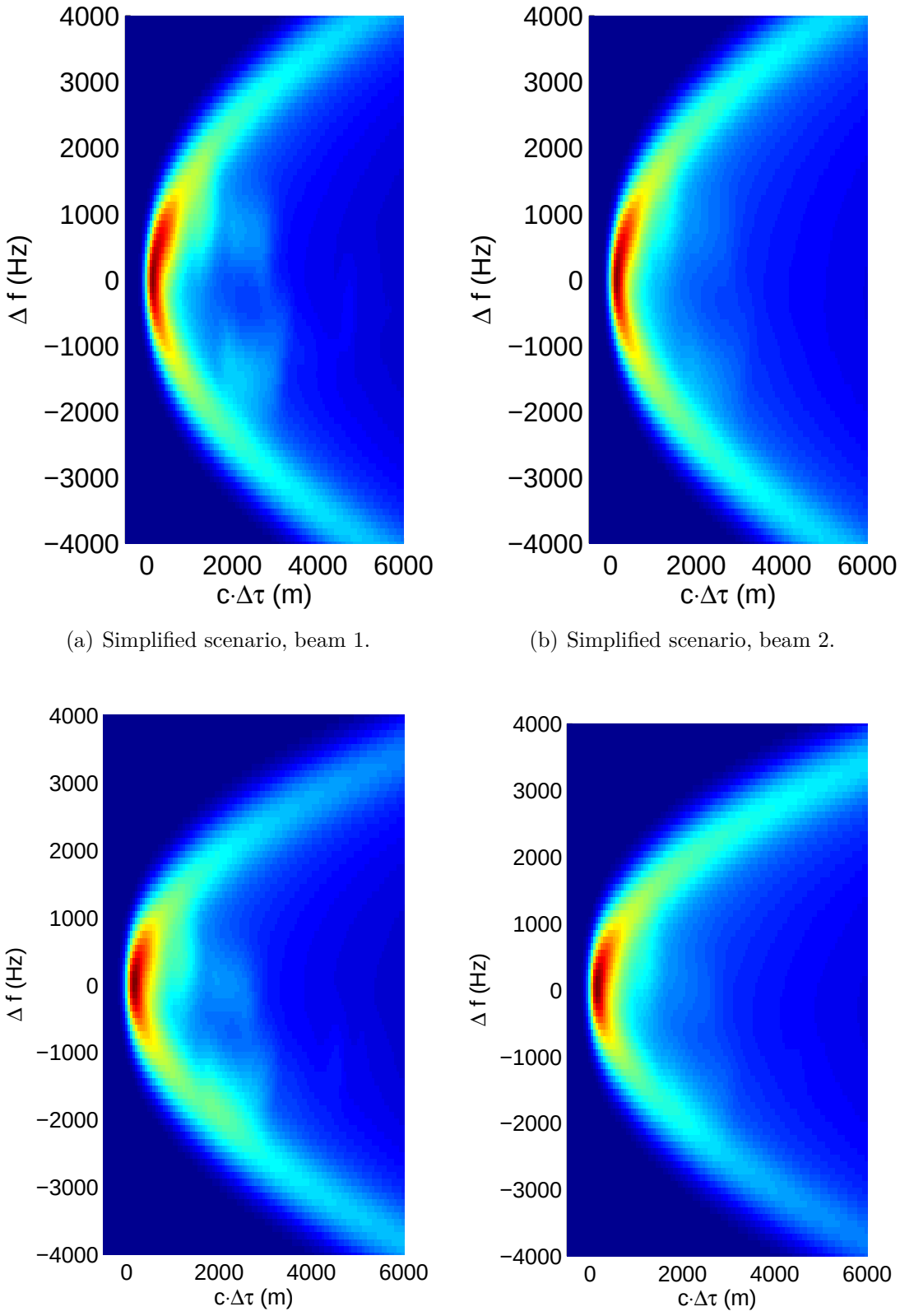

(a) Simplified scenario, beam 1.

(b) Simplified scenario, beam 2.

(c) General scenario, beam 1.

(d) General scenario, beam 2.

Figure 3.7: Delay-Doppler maps with respect to the scenario and antenna beams.

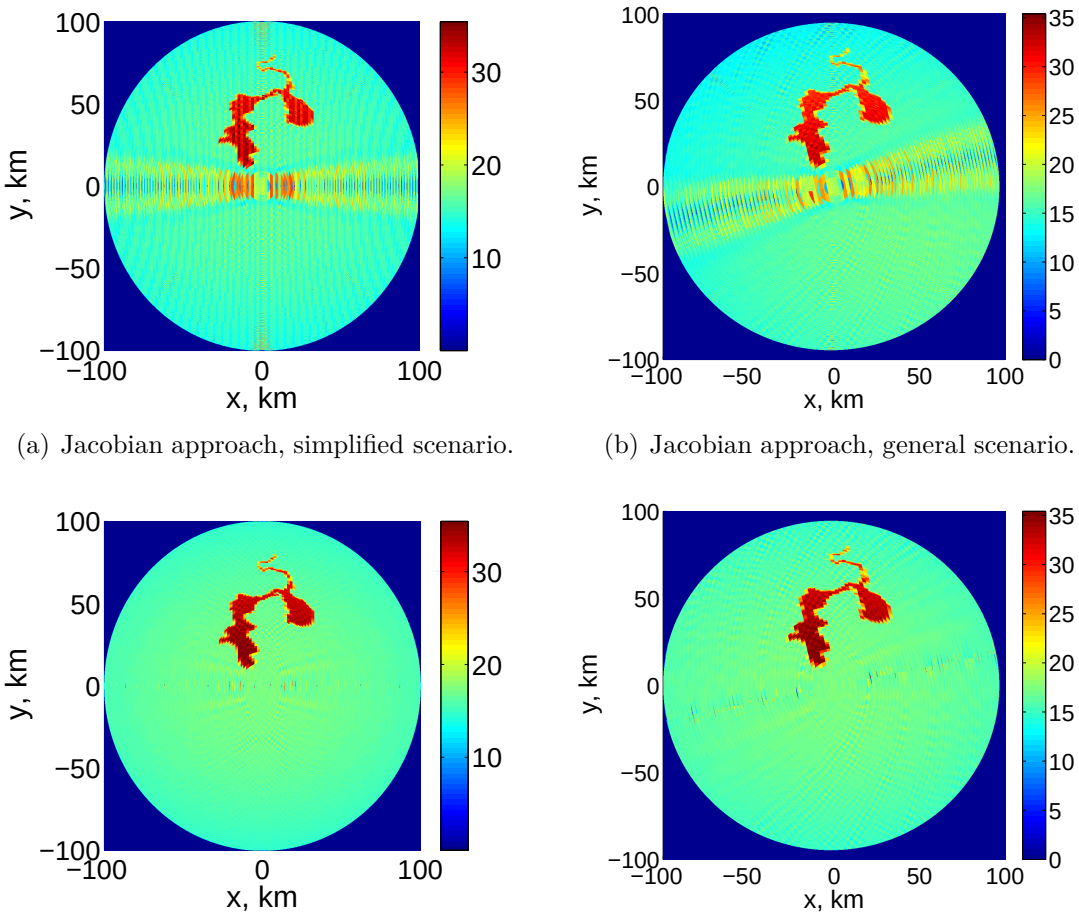

(a) Jacobian approach, simplified scenario.

(b) Jacobian approach, general scenario.

(c) SIA, simplified scenario.

(d) SIA, general scenario.

Figure 3.8: Scattering coefficient retrieval results.

can be observed in Fig. 3.7, the oil slicks in the general scenario DDMs are slightly twisted compared to that of the simplified scenario DDMs. This is because of the change of the Doppler distribution caused by the different geometries between the two scenarios. Moreover, the two DDMs of the scenario have different power distributions as the result of the two antenna beams illuminating two different areas.

3.4.1 Retrieval Result of Scattering Coefficient Distribution

Scattering coefficients were determined from the DDMs using both the Jacobian approach and the SIA. The corresponding results are shown in Fig. 3.8. The directions

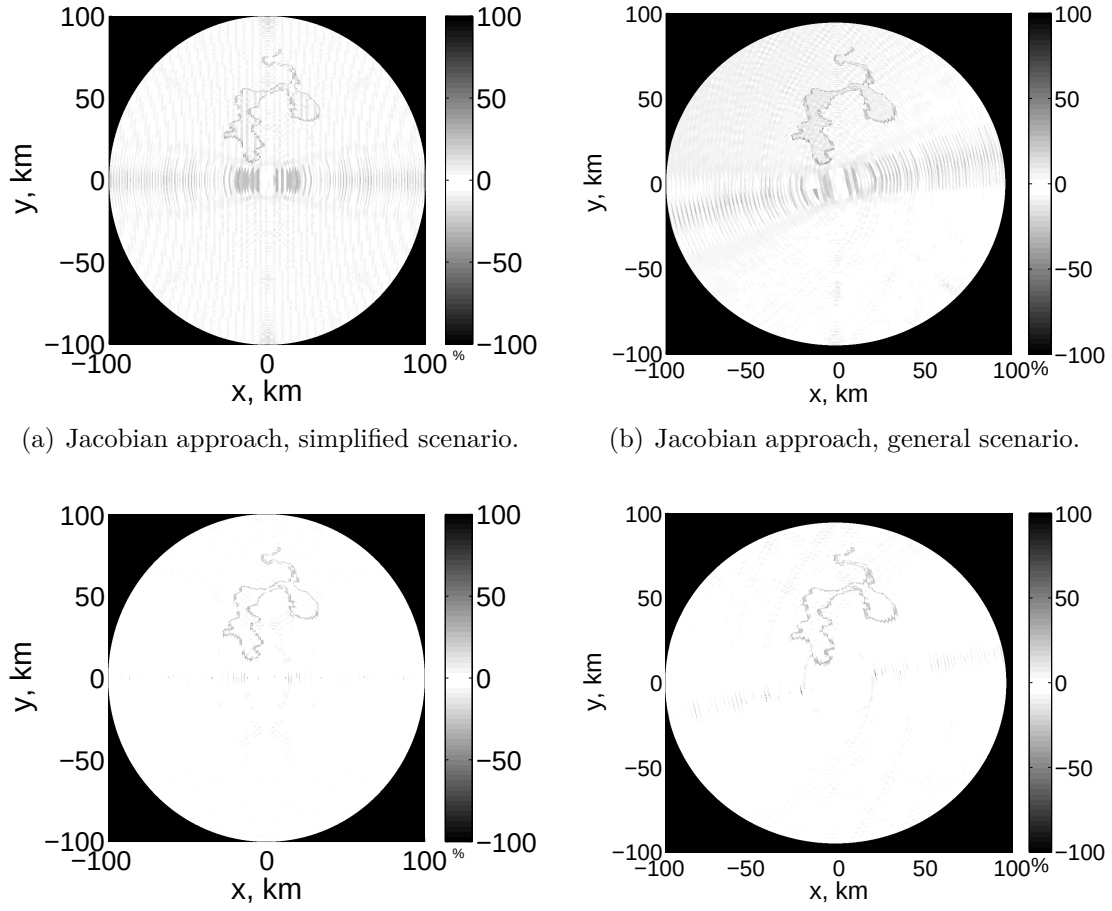

(a) Jacobian approach, simplified scenario.

(b) Jacobian approach, general scenario.

(c) SIA, simplified scenario.

(d) SIA, general scenario.

Figure 3.9: Error distribution maps.

of the ambiguity free lines are different when comparing the results of the simplified scenario with those of the general scenario.

One thing worthy of note is the Jacobian approach applied in this retrieval does not rely on the algorithm proposed in [39] to calculate $\vec{\rho}(\Delta\tau, \Delta f)$ for each DD point. Rather, the Doppler frequency shift and C/A delay of each spatial point is determined precisely using the approaches in [7]. Theoretically, this modification will slightly increase the accuracy but will require more computation time.

The error maps of the two approaches are shown in Fig. 3.9. It can be seen that the error of the retrieval results in the SIA and the Jacobian approach are, in general,

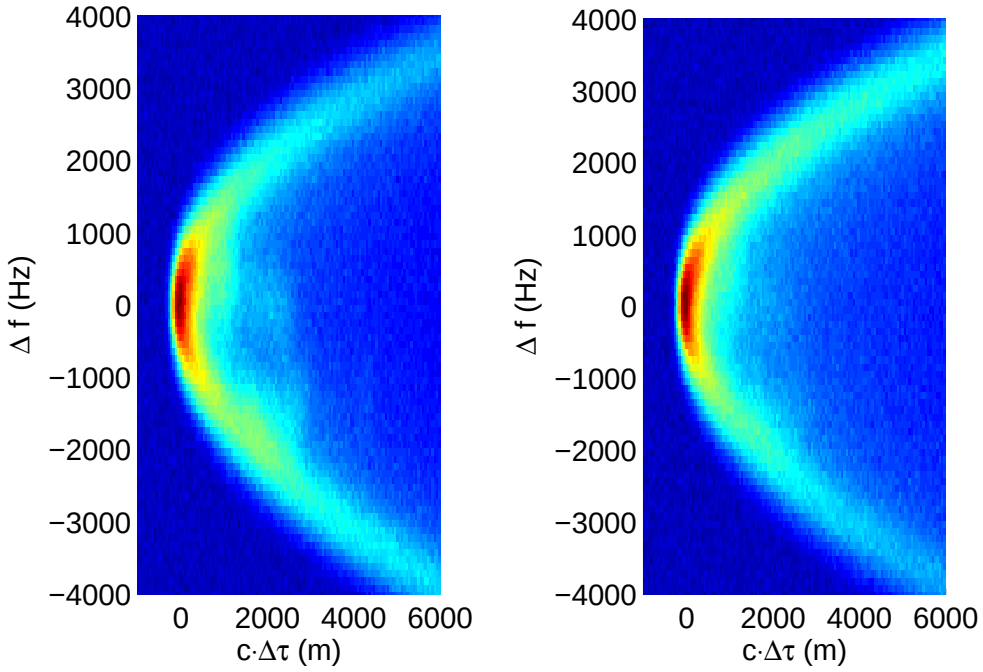

(a) Beam 1 (b) Beam 2

Figure 3.10: Delay-Doppler maps with the SNR_p=18.5 dB.

below 5% and 10%, respectively. Nevertheless, the error increases at the boundaries of the oil slicks, as the distribution details are lost when mapping from the low-resolution DD domain to the high-resolution spatial domain. Particularly, the major difference between the two retrieval results is in the area surrounding the ambiguity free line. It can be observed that the SIA reduces the error of the Jacobian approach from 20% to less than 5%. By using the SIA, the calculation is conducted over the entire x-y plane with no such approximations made.

To illustrate the performance of the two approaches, no noise was introduced during the initial simulations of oil slick detection discussed above. Next, the technique proposed in this research is validated with the presence of noise where the distortion correction method discussed in Section 3.2.1 is employed. The corresponding DDMs incorporating noise are shown in Fig. 3.10. The integrated noise has an SNR_p of 18.5 dB and an absolute SNR of 5.2 dB. The performance of the distortion correction

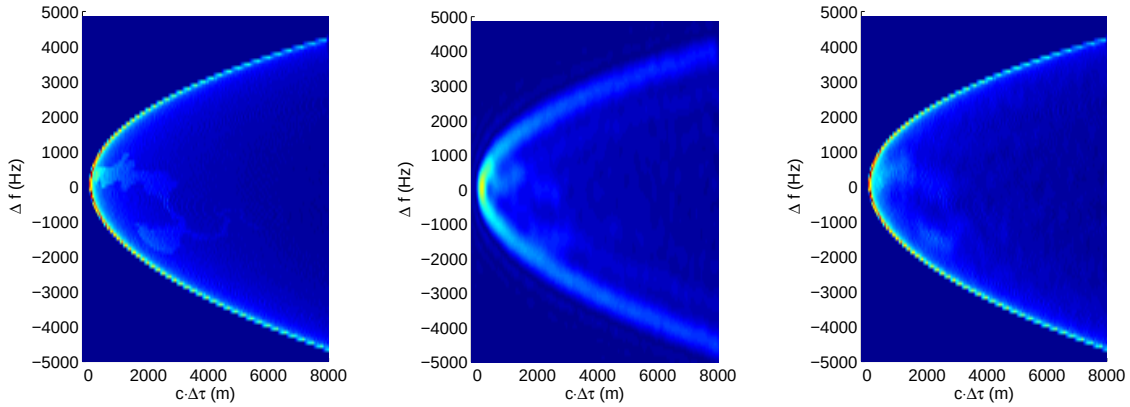

(a) Real distribution.

(b) Retrieved distribution without distortion correction.

(c) Retrieved distribution with distortion correction.

Figure 3.11: Σ of the oil-slicked surface in the DD domain.

shown in Fig. 3.11, includes the original Σ, the result Σ_γ directly obtained by the CLS filter, and the result Σ'_γ obtained after the distortion correction. Compared to Fig. 3.11(a), Fig. 3.11(b) clearly shows the distortion caused bty the Laplacian operator. Particularly, the inaccurate areas appear to be horseshoe shaped across Fig. 3.11(b). On the other hand, although, on closer inspection, noise effects can still be found, the distortion-corrected result in Fig. 3.11(c) shows better matches with Fig. 3.11(a) especially at the oil-free area.

Scattering coefficients were then obtained using the spatial integration approach and the Jacobian approach. The corresponding results are shown in Fig. 3.12. Both scattering coefficient distributions, with and without ambiguity, are obtained in the case of the SIA. For comparison, the result without distortion correction is also demonstrated here.

As can be observed in Fig. 3.12(a), two oil slick candidates occur in the results obtained. Since each point in the DD domain corresponds to two positions in the spatial domain, the ambiguity problem appears when using only one DDM. Since the intensities of the scattering coefficients and shapes of the two oil slick candidates

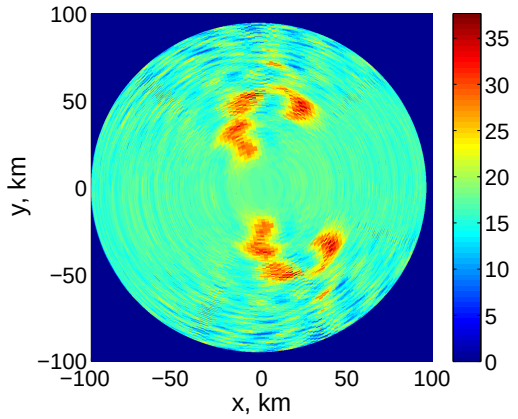

(a) One DDM, SIA, with distortion correction.

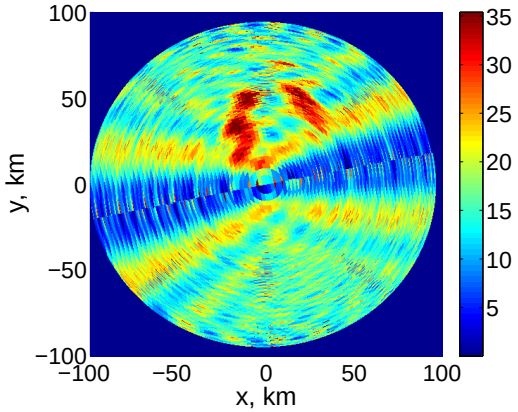

(b) Two DDMs, SIA, without distortion correction.

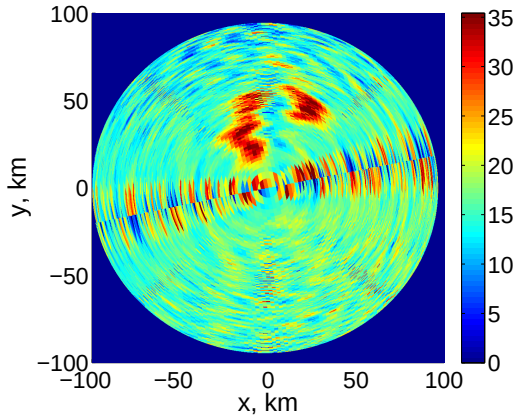

(c) Two DDMs, Jacobian approach, with distortion correction.

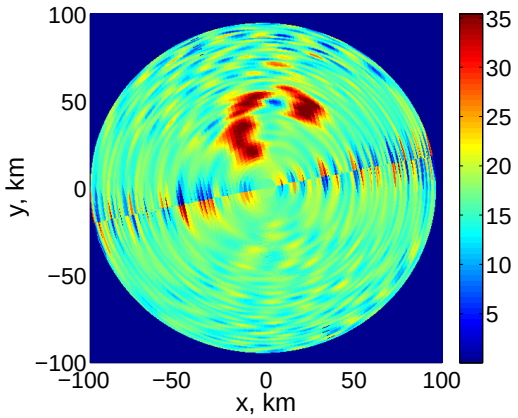

(d) Two DDMs, SIA, with distortion correction.

Figure 3.12: Retrieved scattering coefficient distribution.

are almost the same, the actual location of the oil slick is ambiguous and cannot be determined without additional information. As for the results using the 2-DDM cases, the ambiguity problem is better resolved. The effectiveness of this approach lies in the receiver generating two separate DDMs using two antenna beams. This is achieved by using two left-hand circularly polarized downward-pointing antennas to collect two DDMs simultaneously from different viewing angles.

The result without distortion correction can be observed in Fig. 3.12(b). The difference between the results with and without distortion correction can be observed more clearly in the error map of the retrieval result in Fig. 3.13. The scattering coefficients retrieved from Σ_γ in Fig. 3.12(b) tend to be lower than their actual values in areas near the ambiguity free line. Outside the small value region, there is one high value strip at each ambiguity free zone. When intersecting with a strip, the retrieved oil slicked extent is distorted in this example and is likely to be distorted in other cases. Thus, the main purpose of the distortion correction is to reduce the strip shaped inaccurate area, and hence increase the performance of oil slick detection.

The difference between the results of the SIA and Jacobian approaches with the presence of noise is similar to that without noise. The result from the SIA shows an improvement in terms of the size of the region prone to error around the ambiguity free line. Also, the SIA performs slightly better in reproducing the details of the oil slick. However, it should be noted that the reason for the lower accuracy of the Jacobian approach is due to the mathematical approximations used to improve time efficiency. While scattering coefficients obtained using the SIA are more accurate, the lower computational expense of the Jacobian approach should also be considered when selecting the appropriate algorithm.

With the SNR_p of 18.5 dB, the error of the results from the SIA is, in general, below 30%. Even after the distortion correction, Fig. 3.13 shows higher inaccuracy

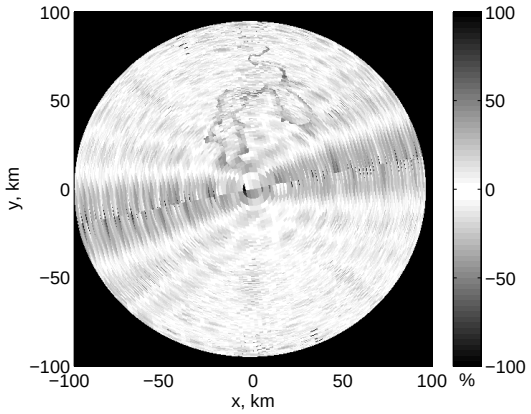

(a) SIA, without distortion correction.

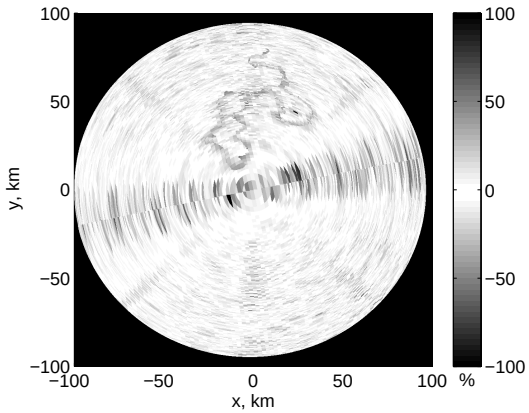

(b) Jacobian approach, with distortion correction.

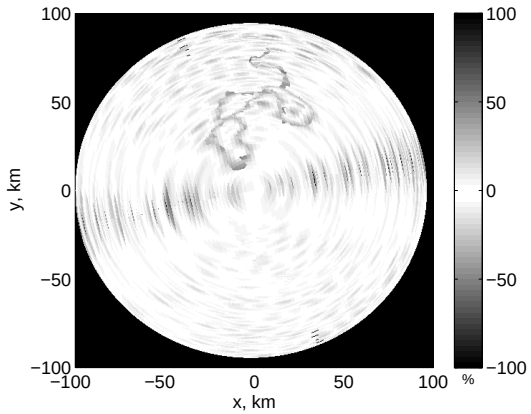

(c) SIA, with distortion correction.

Figure 3.13: Error distribution maps.

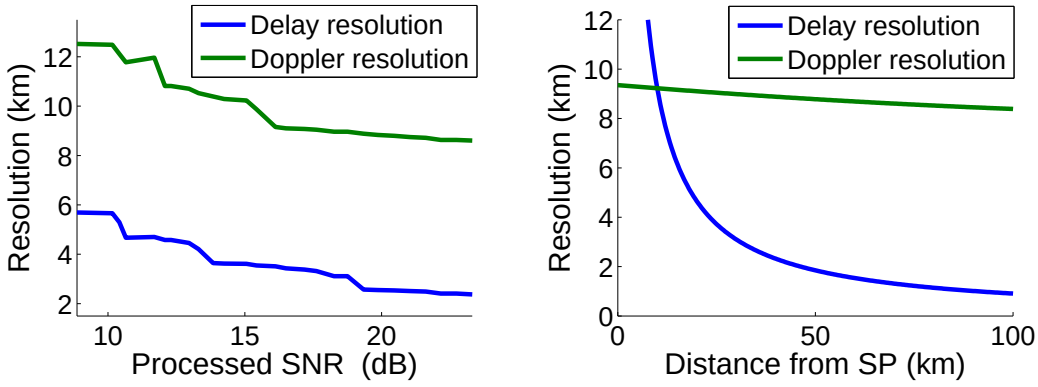

(a) (b)

Figure 3.14: Spatial resolution: (a) at the distance of 30 km from the SP. (b) at an SNR_p of 18.5 dB.

near the ambiguity free line than in the rest of the area. This is likely because the presence of noise causes generation of more than one solution of Eq. (3.21) and Eq. (3.22) at those points.

3.4.2 Resolution Properties

The spatial resolution of the retrieved result is determined using the process described in Section 3.3.2. It should be noted that when mapping a specific resolution term into the spatial domain, the spatial resolution is affected by the location of the projection. When projecting the resolution term near the SP, the obtained spatial resolution is low. When projecting the term away from the SP, the obtained spatial resolution becomes higher. Thus, the spatial resolution is determined with respect to both SNR_p and the distance between the projection location and the SP. The corresponding determined resolutions are shown in Fig. 3.14. Fig. 3.14(a) shows the resolution of the surface regions at a distance of 30 km from the SP under different SNR_p levels. Fig. 3.14(b) shows the resolution at an 18.5 dB SNR_p at different distances from the SP. This SNR value corresponds to the 1 s incoherent correlation time.

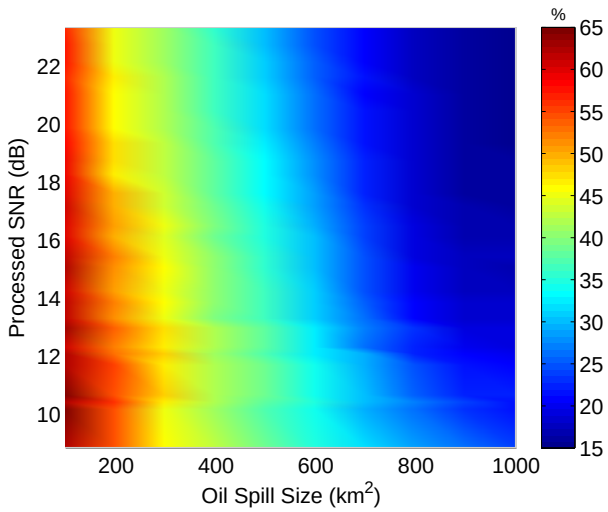

Figure 3.15: Error of Retrieved Scattering Coefficient using the SIA.

From Fig. 3.14(a), it follows that both the delay resolution ΔR_τ and the Doppler resolution ΔR_f becomes better with respect to the SNR_p. At a distance of 30 km, ΔR_τ changes from 2.4 to 5.7 km and ΔR_f changes from 8.6 to 12.5 km, respectively. Fig. 3.14(b) demonstrates that ΔR_τ decreases significantly when moving away from the SP, whereas ΔR_f is relatively stable with respect to that distance. Given both a distance of 30 km and a SNR_p of 18.5 dB, the corresponding ΔR_τ and ΔR_f are 3.1 and 9.0 km, respectively.

3.4.3 Inaccuracy of Scattering Coefficient Retrieval Result

In order to characterize the performance of the SIA more comprehensively, the average inaccuracy of the retrieved scattering coefficient distribution over the oil-spilled area is determined with respect to the SNR_p and the size of the oil slick. The corresponding retrieval inaccuracy result is shown in Fig. 3.15.

As can be observed from Fig. 3.15, the value of the processed SNR are inversely correlated with the size of the oil spill to achieve the same accuracy level. For example, to ensure $\alpha < 50\%$ the size of the spill must be larger than 300 km^2 when the SNR_p

ranges lower than 18 dB, while this size becomes only 200 km^2 for SNR$_p$ ranges from 18 to 23.6 dB. Since the coverage area of oil spill usually changes with time, a model is used here to compute total slick area with respect to oil volume and time [59]

$$A_s = 2270 \left[\frac{\Delta\rho}{\rho_0}\right]^{2/3} V^{2/3} t^{1/2} + 40 \left[\frac{\Delta\rho}{\rho_0}\right]^{1/3} V^{1/3} U^{4/3} t \tag{3.27}$$

where A_s is the area of the slick (m^2); U is the wind speed (Knot); V is the volume of spill (barrel); t is time (min); ρ_0 is oil density (g/cm^3); $\Delta\rho$ is the density difference between water and oil.

By April 25, 2010, the Deepwater Horizon oil accident had leaked for 5 days at a rate of 62000 barrels/day [60]. By applying Eq. (3.27) to this accident, the calculated oil slick size is 1135 km^2. This matches the size determined using the satellite observation (1030 km^2).

Large scale oil spills have huge impacts on the ocean environment, but small scale oil spills cannot be ignored. They too can have significant environmental impacts. Actually, one of the largest annual contributors of oil pollution is operational discharges of ships [61]. Thus, the time it takes to detect oil spills on a small scale using the proposed technique is also investigated here. Assume an oil spillage of $V = 32$ barrels (1000 gallons); $\rho_0 = 0.8$ g/cm^3 and $U = 21$ Knots (10 m/s). Using Eq. (3.27) it can be determined that it takes the spill 23 days to reach the size of 200 km^2 to be detectable. Thus, it would be difficult to use space-based GNSS-R technology to effectively monitor current operational discharges from ships. With the large spatial and temporal coverage, this technique is more suitable for large scale oil slick detection. To improve its performance for detecting spills on smaller scales, the improvement of the scattering coefficient retrieval resolution is critical. This can be achieved by using signals modulated by the Precision code or improving the SNR$_p$ in

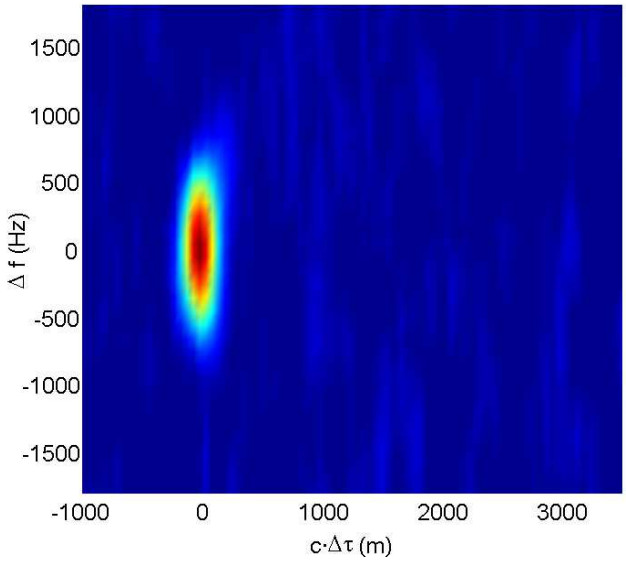

Figure 3.16: Measured DDM at 15.4 s.

the measured DDM.

A preliminary demonstration of applying this oil slick detection technique to real space reflected DDMs is shown below.

3.5 Applying the Technique to Satellite Data

Since no GNSS-R datasets over oil contaminated sea surfaces is available, a dataset collected over land is employed for providing a preliminary validation of the concept. The GNSS-R land dataset used here was collected by the UK-DMC satellite over the mid western USA, near Omaha City on December 7, 2005. The data collected at second 15.4 of the 20 second collection was selected as an example, and a DDM was generated using an incoherent correlation processing time of 100 ms. This DDM contains a strong peak as shown in Fig. 3.16. By comparing Fig. 3.16 with Fig. 3.10, it is found that the area with relatively high power in the DDM over land is smaller than that of the DDMs over ocean. The reason may be that the variation of the

scattering directions produced by the stationary land is less. Thus, it is more difficult to distinguish surface characteristics over the illuminated area far from the specular reflection point [62]. The corresponding scattering coefficient distribution retrieval is shown in Fig. 3.17(a).

In order to validate the deduced scattering coefficient distribution, a reference topography map from the U.S. Geological Survey is used. By knowing the location of the SP, the map of the area of interest is cropped and shown in Fig. 3.17(b), in which the dashed line indicates the ambiguity free line on the iso-height contours. $F1$, $F2$ indicate the relative flat regions, and $R1$, $R2$ denote rougher regions. As can be seen from Fig. 3.17(b), the SP crossed the Platte River at 15.4s. River surfaces are usually very flat and the land surfaces surrounding the SP also have relatively low surface slopes. This coincides well with the high scattering coefficients retrieved in the area around the SP. The scattering coefficient not only depends on the surface slopes of the land surfaces, but is also influenced by the geometry of the surface point, transmitter and receiver. Theoretically, for a piecewise flat plane, the peak scattering coefficient occurs at the SP and decreases when the scattering point moves away from the SP. This trend is observed from the result shown in Fig. 3.17(b): a strong peak is seen at the SP, then a lower scattering coefficient ring appears at further locations. It is believed, if the resolution was higher, a smoother reduction process could be observed. There are several spots of higher scattering coefficient at the edges of the illuminated area, which may be the result of rougher terrains at a distance. For example, the rough region $R1$ which crosses the ambiguity free line aligns well with the area with high scattering coefficient. However, since the land data is measured by only one antenna, the ambiguity still exists. Take rough region $R2$ and flat region $F2$ as an example. These two regions have different land features and are symmetrical to each other about the ambiguity free line. The retrieved scattering coefficient is relatively

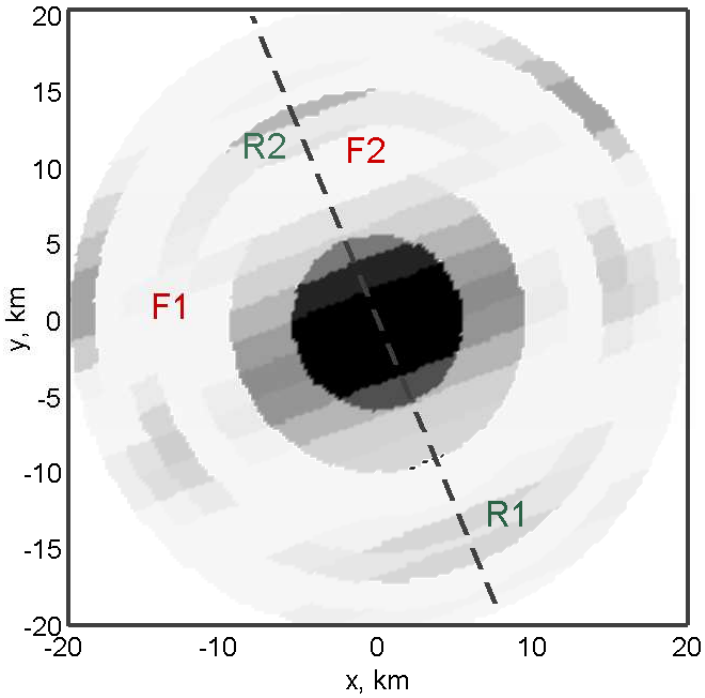

(a)

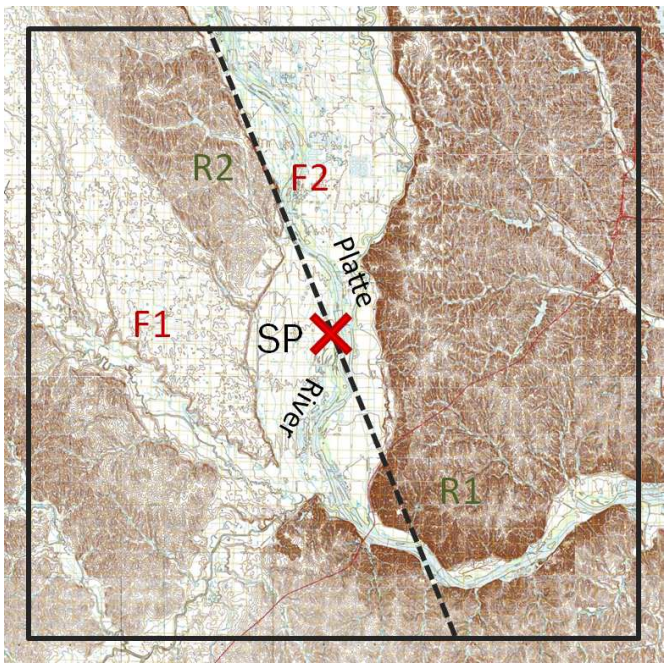

(b)

Figure 3.17: a) Retrieval result of the scattering coefficient distribution. b) Reference topography map. The dashed line indicates the ambiguity free line.

high at some parts of F2 area which is indeed flat. This is due to the fact that the relative high scattering from the rough area in R2 is mapped to its symmetric region in F2 because of the ambiguity. These type of errors resulted due to the ambiguity problem being unresolved with the DDM produced when using only a single antenna. It can be observed that the rough region to the north of $R1$ on the reference map could not be distinguished in the result. There are some reasons that could lead to the discrepancies between the result and the reference map. For example, the topography map is showing large scale contours with the interval of 10 m, while the small scale roughness (surface cover) will also have a significant effect when a 19 cm L1 signal is reflected from similar real land surfaces. It should also be noted that the scattering mechanisms between land and ocean could be significantly different. A rough ocean can be generally modelled using a surface slope distribution and a diffuse scattering assumption. For land this may not be the case, as irregular land surfaces may produce mixed diffuse and coherent reflections across roughness areas not easily modelled as a constant slope probability function.

In order to better mitigate the effect of noise on the DDM, a value larger than 0 was chosen for the CLS weight parameter γ in Eq.(3.3). This somewhat reduced the adverse effect of noise in retrieving Σ. By increasing γ, the noise effect is reduced at a cost of losing land surface details.

Again, it should be noted that the purpose of applying the technique to reflections from land is to validate the scattering coefficient recovery approach for oil slick detection. In fact, of all the aforementioned factors that might cause errors in the results, only the one caused by noise would affect the retrieval result when conducting oil slick detection using the proposed approach. In addition, since the high power region in DDMs over sea surfaces are much larger, this will enable an easier observation of the surface slope differentials for oil spill detection.

3.6 General Chapter Summary

This chapter presents a new method for GNSS-R oil slick detection. The primary contribution of this research is the increase of the accuracy of the scattering coefficient retrieval using two modifications: (1) a spatial integration approach was used to reduce errors near the ambiguity free line and to allow for detailed mapping of non-uniform slope distributions across the surface, and (2) a distortion correction was proposed to reduce the inaccuracy caused by the CLS filter during the DDM de-blurring process. Moreover, this work suggests some practical recipes for the previously proposed two-beam ambiguity solution [40] and demonstrates this solution in a mathematical way by reducing the problem to a system of two linear equations. Finally, the oil slick detection approach was shown to be valid under general reflections geometries which increases the applicability of the approach.

To validate the modifications of the oil slick detection algorithm, an oil-spill detection example is conducted based on the Deep Water Horizon accident in the Gulf of Mexico in 2010. The anticipated improvement has basically been achieved in the simulated demonstration. Following that, a comprehensive test of this technique is conducted to investigate its accuracy and resolution with respect to various SNR levels and oil slicks sizes. A further validation of the concept is then conducted by obtaining the scattering coefficients associated with a space-based GNSS-R land data set. Although the scattering coefficient distribution thus obtained shows differences in details with the reference map, the distributions essentially match with each other from a general perspective.

Chapter 4

Sea Surface Wind Retrieval from GNSS Delay-Doppler Map Using Two-dimension Least-squares Fitting

In this chapter, the algorithm to generate DDMs under general scenarios is applied to retrieve sea surface wind speed and direction using a two-dimensional fitting. This chapter is organized as follows: Section 4.1 describes the new model fitting approach. The corresponding results are provided and discussed in Section 4,2, and a conclusion is made in Section 4.3.

4.1 2-D Fitting Methodology

To retrieve the parameters of interest, an appropriate model that matches the measured DDM should be chosen. The classical (Z-V) model of the DDM in Eq. (2.1)

is also employed here. In this research, the mean square slope is calculated using the clean sea surface model proposed by Cox and Munk [63] with empirical modification for the L band GNSS-R signals [50] given as

$$\begin{aligned} \sigma_u^2 &= 0.45 \cdot (0.00 + 3.16 \cdot 10^{-3} f(U_{10})) \\ \sigma_c^2 &= 0.45 \cdot (0.003 + 1.92 \cdot 10^{-3} U_{10}) \end{aligned} \tag{4.1}$$

where U_{10} is the wind speed at 10 m height from the surface. $f(U_{10})$ is given as

$$f(U_{10}) = \begin{cases} U_{10}, & \text{for } 0.00 < U_{10} \leqslant 3.49 \\ 6\ln(U_{10}), & \text{for } 3.49 < U_{10} \leqslant 46 \\ 0.411 U_{10}, & \text{for } 46 < U_{10} \end{cases} \tag{4.2}$$

By employing these models, the DDM may be simulated under different wind conditions. The generated DDM that best matches the measured DDM is used to estimate the wind information [64]. To quantify the residual error between the two DDMs, the LS fitting is employed in this research. The LS cost function is defined as:

$$\begin{aligned} &\varepsilon(U_{10}, \varphi_0) = \\ &\sum_{\Delta\tau, \Delta f} [a\Big\langle |Y(\Delta\tau - \tau_m, \Delta f - f_m, U_{10}, \varphi_0)|^2 \Big\rangle_s - \Big\langle |Y(\Delta\tau, \Delta f)|^2 \Big\rangle_m]^2 \end{aligned} \tag{4.3}$$

where the subscripts s and m of $\langle |Y(\Delta\tau, \Delta f)|^2 \rangle$ indicate the simulated and measured DDMs, respectively; $\Delta\tau$ and Δf denote the delay and Doppler shift, respectively, and τ_m and f_m are the associated offsets used in the simulated DDM to align the horseshoe shape of the measured DDM to that of the simulated DDM. Since the noise floor of the simulated DDM is zero, the one in the measured DDM needs to be removed before the 2-D fitting. The noise floor can be calculated over the region of delays where no

signal is present (i.e., C/A delays smaller than that of the SP) for each measured delay waveform [17]. The noise floors are then subtracted from the associated delay waveforms in the measured DDM before model fitting. The generated and measured DDMs are then normalized using their peak values. The normalized measured DDM can be contaminated by noise at the highest-intensity point. Thus, a scaling factor a is used for fitting the modeled DDM magnitude to that of the measured DDM. The range of a is set empirically from 0.9 to 1.1. Since the DDM points with low intensity are more sensitive to the noise, thresholding is used here to exclude these points from the 2-D LS fitting.

Increased computation load is resulted from the extra dimension in the 2-D LS fitting compared with 1-D fitting. A step-size-varying iteration technique similar to that in [65] is used to reduce the computational cost during seeking the optimal a in the iteration, which is referred to as 'variable step-size iteration'. The flow chart of the variable step-size iteration is shown in Fig. 4.1, in which the subscript l and h indicate the lower and upper bounds, respectively, and δ denotes the step-size. ϵ_s represents the minimum value of ϵ and T_a (= 0.01 here) is a pre-defined step-size lower bound to terminate the fitting process. This technique initially involves using a wide search range and a coarse resolution for a to obtain a sub-optimal set of parameters (a^*, τ^*, f^*, U_{10}^*, φ_0^*). Next, the search is narrowed around a^* and a smaller search step-size δ_a is used. The search continues until the step size is reduced to be lower than T_a. The details in the variable step-size iteration are given below:

1. Set the range of a from $a_l = 0.9$ to $a_h = 1.1$ with a relatively large $\delta_a = 0.05$.

2. Generate a set of modeled DDMs for each combination of (a, τ, f, U_{10}, φ_0).

3. Determine the optimal value for the model parameter a, i.e., a^*, which produces the least error between the modeled DDM and the measured DDM.

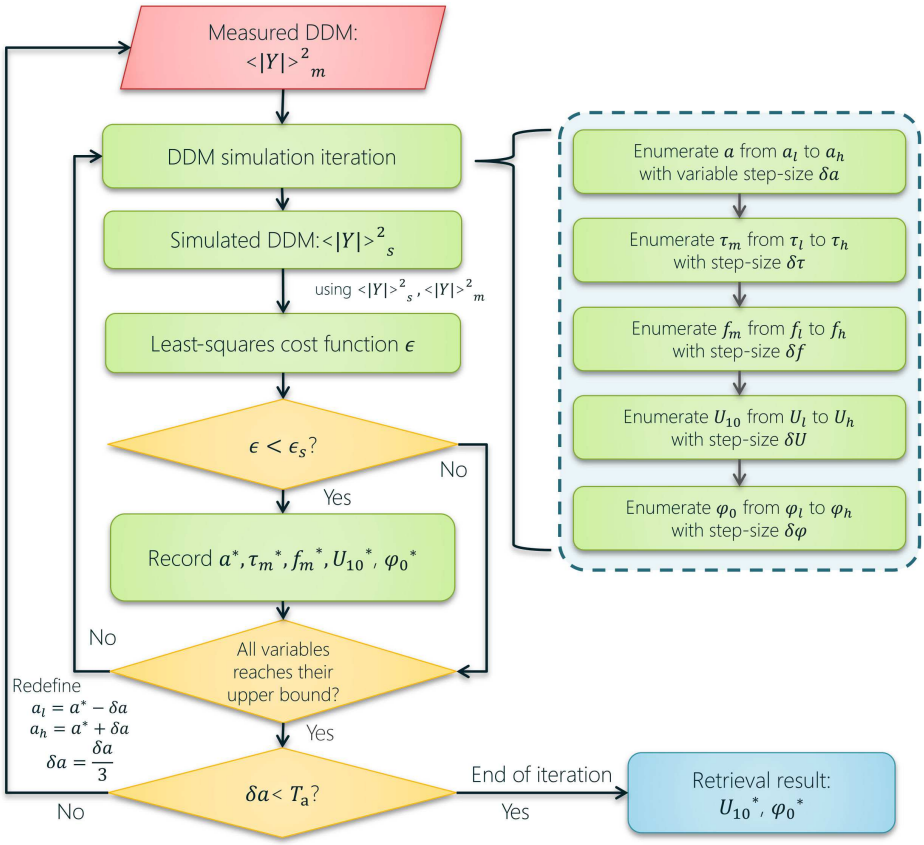

Figure 4.1: Flow chart of variable step-size iteration.

4. Narrow the search range of a to $a_l = a^* - \delta_a$ and $a_h = a^* + \delta_a$, and reduce the step size δ_a by a factor of 3.

5. Repeat steps 2) - 4) until $\delta_a < T_a$.

6. The iteration is terminated. U_{10}^* and φ_0^* obtained from the last search are considered as the retrieval result.

In this paper, only the step-size of a is varied during the iteration. This is because 1) the cost function has an absolute minimum with respect to a; 2) the cost function may have local minimums with respect to wind speed and direction, so it's better to use fixed step-sizes for search; 3) the step-sizes of the delay and frequency offset are fixed, and determined by the sampling rate and the Doppler bin of the measured DDM.

4.2 Results

In order to validate the 2-D LS fitting method, the measured DDM is generated using three datasets (R12, R21 and R35) collected by the UK-DMC satellite over the North Pacific Ocean. The receiver on the UK-DMC satellite receives scattered signals using a down-looking antenna that steers 10 degrees "behind" the satellite (the opposite direction of the velocity of the receiver) using a yaw rotation of the spacecraft [17]. Since the antenna senses a large area (the 3-dB footprint is roughly 1000 km $\times$ 200 km as shown in Fig. 3.3), the receiver usually receives signals from more than one GPS satellite. After choosing the appropriate signal in terms of its acquisition SNR and grazing angle, the received signals can be processed using both navigation information provided by the UK-DMC GNSS-R receiver and GPS satellite information provided by the International GNSS Service (IGS). More specifically, the signal needs

to be down converted, sampled and coherently correlated with the locally generated Pseudo Random Noise code that belongs to the corresponding GPS satellite from which the chosen signal comes. Each correlation generates a 1-D delay waveform with a specific Doppler frequency. These steps are similar to signal processing of typical GPS receivers. Particularly, this correlation helps to recover the original signals as well as separate signals transmitted from different GPS satellites. In this research, the aforementioned signal processing steps are conducted using the open source Software Receiver in [44]. A 1 ms coherent correlation time is also chosen here. The obtained delay waveforms are usually significantly contaminated by speckle noise, which is due to the various carrier phases from different reflecting surface facets. Here, this effect is mitigated by incoherently accumulating the received signals over consecutive coherent correlations. More specifically, the generated waveforms must be aligned and averaged over time with the appropriate phase offset and Doppler frequency shift in order to recover the true signal power profile. The longer the incoherent interval is, the lower the variance of the noise in the waveform will be [5]. Since the performance of the model fitting can vary considerably depending on the amount of the noise present, in this research the interval is set as 18 seconds, which is almost as long as the 20 second duration of the data collection. Since the transmitting and receiving satellites are rapidly moving at a speed of several km/s when collecting the data, the associated change of the system dynamics must be carefully taken into account [17]. It is important to note that the incoherent correlation time is 1 s or less in most existing GNSS-R remote sensing applications. In these cases the Doppler frequency shifts of several 10's of Hz are negligible. However, with a correlation time of more than 15 s, the change of the Doppler frequency must be considered. Then, the DDM may be obtained by simply combining these waveforms according to these frequencies. Lastly, the noise floor, which varies with Doppler frequency, needs to be removed. The

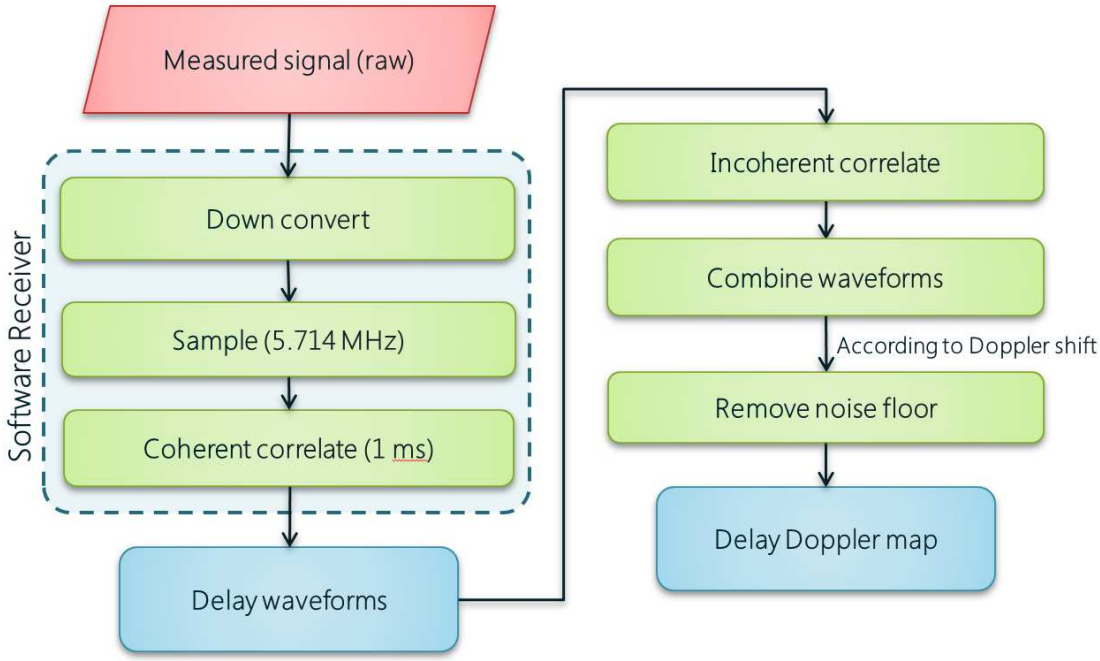

Figure 4.2: Signal processing flowchart of UK-DMC raw datasets.

signals with C/A delays smaller than that of the SP are considered to be pure noise. Thus, for each delay-waveform the noise floor is determined by averaging these noise signals. The signal processing flowchart is shown in Fig. 4.2.

Theoretically, long incoherent correlation intervals could always guarantee low noise levels in DDMs. However, in actual practice the interval has some limitations and its length can not be set arbitrarily. As the geometry of transmitter-receiver changes during data collection, the location of the horseshoe shape changes in the Delay-Doppler (DD) domain. However, the measured DDM only covers a fixed range of the Doppler shift and delay. As a result, some portion of the horseshoe shape may fall outside of the DD range for the data collected at the end of every 20-second recording period, e.g., dataset R12 at 19-20 s. Such an incomplete DDM cannot be used for incoherent averaging. Accordingly, the incoherent averaging time is determined based on this criterion.

Simulated DDMs are generated for wind speeds from 1 m/s to 16 m/s with a

step-size of 1 m/s. Since wind direction ambiguity is removed based on the *in-situ* information, the wind directions only need to be chosen from 0° to 180° or 180° to 360° with respect to the x-axis. Fig. 4.3, Fig. 4.4 and Fig. 4.5 show the corresponding measured and modelled DDMs of the R12, R21 and R35 dataset, respectively. As can be seen in the figures, after an 18 s incoherent correlation, the simulated DDMs show clear horse-shoe shapes. The simulated and modelled DDMs seem highly correlated, while close inspection reveals divergence in the peak-value area, particularly for the R21 dataset. Since, theoretically, the influence of the noise should be relatively small in that area, the reasons for this problem are likely to be the following: 1) inaccuracies in the Doppler-frequency shift and delay due to the bias in the receiver clock [17] and 2) the antenna pattern applied in the DDM simulation is only an approximate UK-DMC antenna pattern. Without access to all the necessary information to estimate the bias, it would be difficult to eliminate the inaccuracy caused by receiver clock. To balance the adverse effect of antenna pattern error, the simulated antenna is adjusted accordingly here. More specifically, the along-track and cross-track half power beam width (HPBW) of the antenna pattern is modified according to the extents of the three DDM measurements. This modification may compensate somewhat for any inaccuracy of the simulated antenna pattern, but it may also result in overestimation of the accuracy that could be achieved using 2-D LS fitting. In the future, no such modification would be required if the antenna pattern of the receiver is precisely calibrated before launch.

The *in-situ* measurement data from the National Data Buoy Center (NDBC) [52] is used as ground truth for comparison. The buoy anemometer is 5 m above the sea level. In order to apply the wind speed to Eq. (4.1), the measured speed is converted to the value at a 10-m height based on a neutral stratification logarithmic law [66]. The corresponding buoy-measured wind direction (clockwise from the true

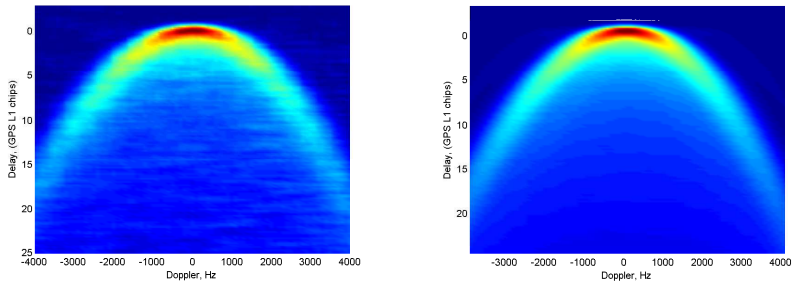

(a) (b)

Figure 4.3: Generated DDMs during 18 s from dataset R12: (a) Measured DDM. (b) Modelled DDM.

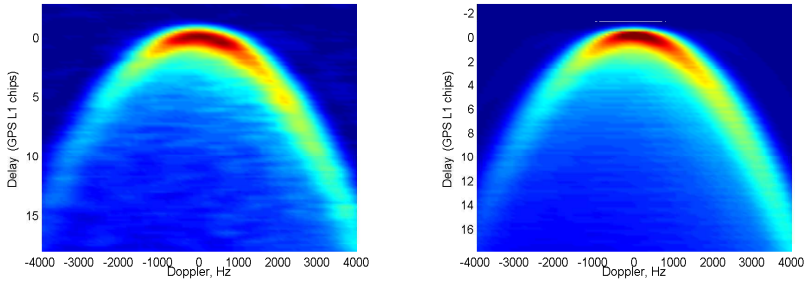

(a) (b)

Figure 4.4: Generated DDMs during 18 s from dataset R21: (a) Measured DDM. (b) Modelled DDM.

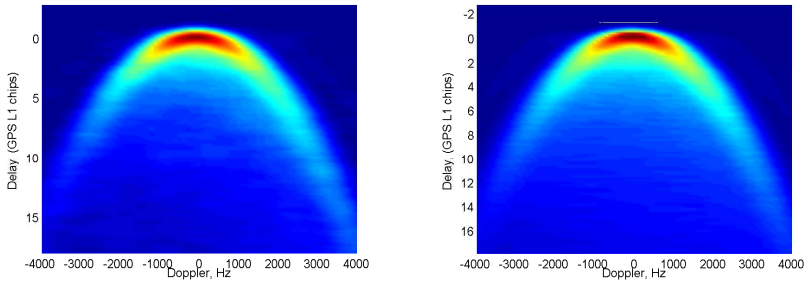

(a) (b)

Figure 4.5: Generated DDMs during 18 s from dataset R35: (a) Measured DDM. (b) Modelled DDM.

Table 4.1: GNSS-R Data Collection Information, Buoy Measurements and Retrieved Wind Field

Dataset Label	PRN	Collection Time	Elevation Angle	Buoy No. (Latitude, Longitude)	Buoy-measured Wind Speed & Wind Direction	Retrieved Wind Speed & Wind Direction
R12	22	7:54 am Nov. 16, 2004	76.7°	46006 (40.754 N, 137.464 W)	8.96 m/s 253°	8.00 m/s 283°
R21	29	9:16 am May 2, 2005	84.5°	51001 (23.445 N, 162.279 W)	4.21 m/s 23°	3.60 m/s 28°
R35	30	7:46 am Aug. 10, 2005	78.4°	46006 (40.754 N, 137.464 W)	5.39 m/s 135°	4.50 m/s 160°

North), converted wind speed and other information of the datasets are shown in Table 4.1. The time differences between the GNSS-R data collections and the *in-situ* measurements are less than 10 minutes for all datasets. Also, the distances between the GNSS-R specular points and the buoy stations are less than 100 km for all three datasets (see Fig. 4.6 which is generated using Google Map). An assumption is made here that the wind is uniformly distributed at the Buoy station, the start point and the end point of the SP for each GNSS-R dataset.

Given that accurate measurements are more likely to be achieved in areas of high SNR, no upper bound is set for thresholding the signal, and a batch of lower bounds are tested to achieve an optimal fitting for wind recovery. The lower limits of the threshold are set from 15% to 60% with respect to the peak value of the measured DDM. Fig. 4.7, Fig. 4.8 and Fig. 4.9 show the corresponding results using the 2-D LS fitting.

As can be observed from Fig. 4.7(a), the retrieved wind speed varies from 6 m/s to 11 m/s depending on the threshold. As the lower limit of the threshold increases, the retrieved wind speed increases. The most accurate result is obtained when the lower limit is chosen between 30% and 51%. For wind direction (with respect to the true North), the retrieved results are in the range of 268° to 313° and they are all larger than the *in-situ* measured value. It can be seen from Fig. 4.7(b) that the wind direction obtained using a threshold with low limit ranges from 24% to 48% is

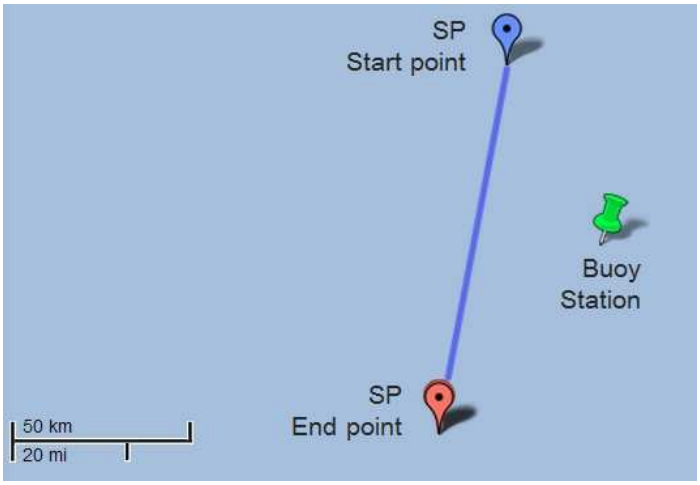

(a) R12

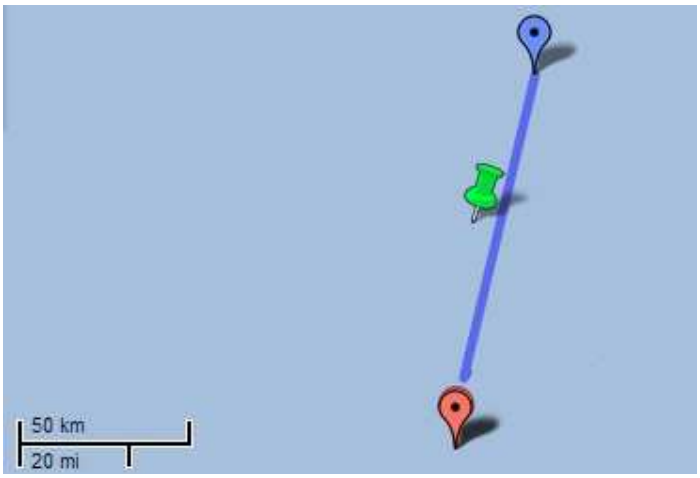

(b) R21

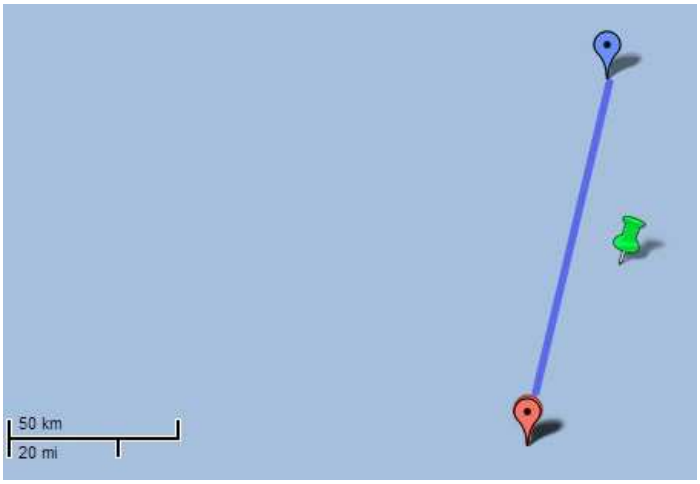

(c) R35

Figure 4.6: The track of specular points during data collection: The marks at top and marks at bottom indicate the starting and ending locations (at 18th second) of the specular points, respectively. The tacks indicate the locations of the NDBC Buoy Stations.

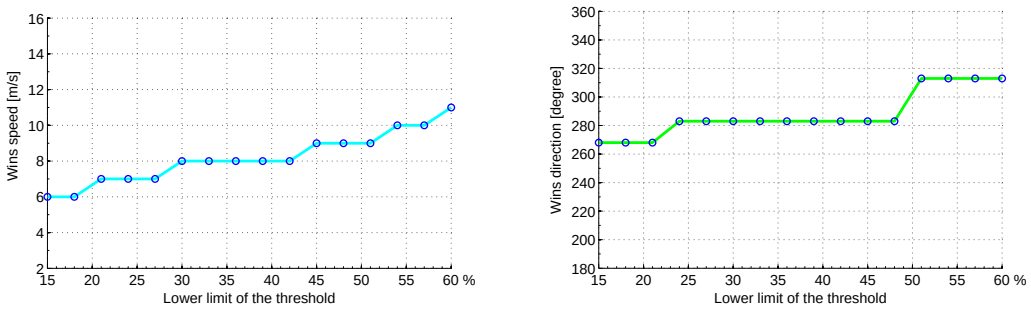

(a) (b)

Figure 4.7: Wind results versus the lower limit of the threshold (R12): (a) Wind speed. (b) Wind direction.

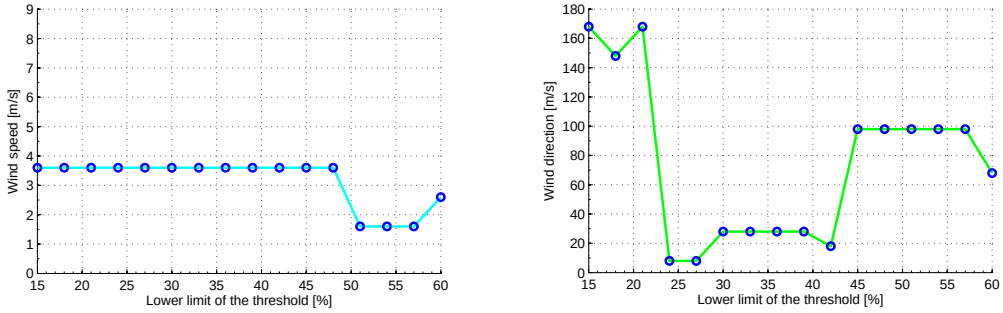

(a) (b)

Figure 4.8: Wind results versus the lower limit of the threshold (R21): (a) Wind speed. (b) Wind direction.

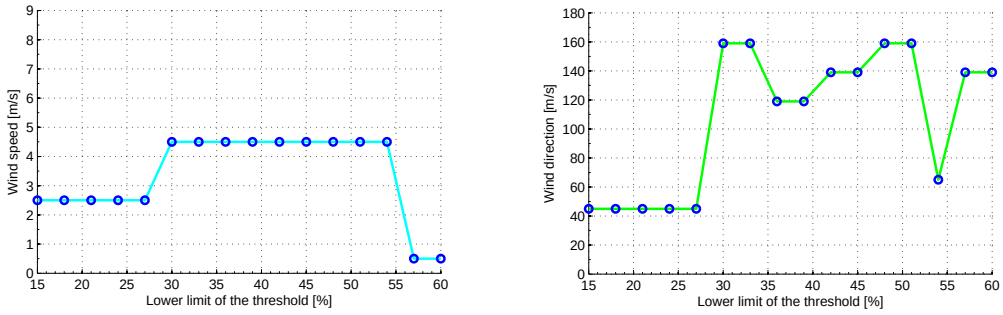

(a) (b)

Figure 4.9: Wind results versus the lower limit of the threshold (R35): (a) Wind speed. (b) Wind direction.

283° which is 30° different from the buoy result. It was found from Fig. 4.7 that the retrieved wind speed and direction from dataset R12 have relatively large errors when the lower limit is greater than 51%, which might be caused by the reduction of the number of points used for fitting. Moreover, the peripheral area of DDMs is more sensitive to wind direction [67] than other portion, and the wind direction accuracy will be reduced if the imposed threshold is too high. Similar results can be observed in R21 and R35 datasets. The optimal thresholds for R12, R21 and R35 are 30% to 48%, 24% to 42% and 30% to 52%, respectively, for which errors of 0.96 m/s and 30° (R12); 0.61 m/s and 5° (R21); and 0.89 m/s and 25° (R35) are obtained. Based on the analysis, the lower limit of the threshold for the 2-D LS fitting is recommended to be chosen from 30% to 42%.

Hence, according to this analysis, the lower limit of the threshold chosen for the 2-D LS fitting should be chosen from 30% to 42%. It is important to note that this approach works better when the sea surface is well-developed by a continuous and consistent wind blowing for several hours. According to the *in-situ* measurements from the NDBC, the wind blew for 2.5 hours at a speed of 7.7 m/s to 9.3 m/s in the direction of 253° to 265° for R12; 3.5 hours at a speed of 3.8 m/s to 5.9 m/s in the direction of 9° to 32° for R21; and 3 hours at a speed of 3.3 m/s to 5.4 m/s in the direction of 120° to 140° for R35 [52]. During the data collection periods of the three datasets, the sea was assumed to be well-developed here.

4.3 General Chapter Summary

In this chapter, a method for retrieving sea surface wind speed and direction by 2-D LS fitting the measured and simulated DDMs is presented. Testing results using the data collected by the UK-DMC satellite validates the algorithm through comparing

them with the *in-situ* wind data. The test also shows the performance of the approach depends on the threshold lower limit of the signal power magnitude in DDMs. An error under 1 m/s in wind speed and 30° in wind direction can be observed when the lower limit is set from 30% to 42%. It is important to note that in this work the simulated antenna pattern is modified for each GNSS-R dataset to reduce the error. Thus, the achieved accuracy might be overestimated here.

Chapter 5

Conclusion

5.1 General Synopsis and Significant Results

In this thesis, research for improving sea surface remote sensing using the Global Navigation Satellite System-Reflectometry (GNSS-R) signals has been presented. Firstly, the detailed simulation process for Delay Doppler Maps of oil-slicked sea surface under general scenarios, of which the elevation angles are not necessary to be 90°, is presented. Secondly, a spatial integration approach is employed to detect oil slicks from GNSS-R Delay Doppler Maps under general scenarios. Finally, two-dimensional fitting is used for sea surface wind speed retrieval.

The main contribution of the detailed DDM simulation process lies in extending the original DDM generating process from a simplified geometric scenario to a general one for oil-slicked sea surfaces. This extension modifies not only the scattering coefficient retrieval approach, but also the DDM simulation approach which provides reference and validation data for the retrieval algorithm development. Most steps of this simulation approach are applicable to various sea states and they are described in more detail than in previous works.

The new method for oil slick detection from GNSS-R Delay Doppler Maps using scattering coefficient recovery offers four significant improvements to previous work. The first improvement is achieved by correcting the distortions due to the CLS filter during the DDM deconvolution process. This correction method can increase the oil slick detection accuracy especially under high noise levels. The second improvement comes from suggesting practical recipes to solve the ambiguity in DDMs by reducing the problem to a system of two linear equations. Although this idea was first proposed in [40], this research presents a more practical recipe with mathematical details for oil slick detection. The third improvement is achieved by bringing the spatial integration approach to scattering coefficient retrieval. Compared to the Jacobian based model, this approach has lower retrieval errors with only a modest cost in additional computation time. The fourth improvement results from the retrieval resolution term of GNSS-R. Using this term, the resolution of the scattering coefficients obtained from deblurred DDMs is determined for the first time. Also, a comprehensive validation is conducted to characterize the performance of the proposed oil slick detection method under different noise levels.

To validate the oil slick detection algorithm, and to compare the performance of the Jacobian approach with the spatial integration approach, an oil-spill detection example is conducted based on the 2010 Deep Water Horizon accident in the Gulf of Mexico. Both the oil slick extent and the corresponding wind field information are taken into account. This simulated demonstration shows the anticipated improvements in the recovery accuracy. In addition, this approach is further verified using real data collected from land surfaces by the GNSS-R receiver loaded on the UK-DMC satellite. The result shows differences in details with the reference map but demonstrates the possibility of remotely sensing the scattering coefficient distribution of land surfaces.

In addition to oil slick detection, wind field retrieval using GNSS-R is also investigated in this research. A new retrieval approach is presented based on 2-dimensional delay-waveform least-squares fitting. The primary contribution to this area is the investigation of the possibility of wind retrieval using 2-dimensional DDMs as well as analysing the performance of this method. Unlike previous methods in which only a 1-dimensional delay waveform is used, all the DDM points with normalized power higher than the threshold are used in the least-square fitting. Wind speed and direction are obtained by adjusting the lower limit of the fitting process. Moreover, a variable step-size iteration is used to increase the time efficiency of the technique. To validate this algorithm, three GNSS-R datasets collected over the North Pacific Ocean are employed. The retrieved wind fields are compared with corresponding *in-situ* measurements provided by the National Data Buoy Center. High correlations are shown between the two for the R35 and R12 datasets collected under steady sea conditions. The wind speed retrieved from R20 is higher than the actual buoy measurement. This is very likely caused by the decaying sea state.

Generally, both oil slick detection and wind field measurements using GNSS-R hold a promising future. In the next section, some suggestions are given for improving these techniques for actual practices.

5.2 Suggestions for Future Work

It should be noted that the diffusive (incoherent) reflection approximation upon which the Z-V model is based may fail for very flat surfaces [42] such as the oil-slicked sea surface of relatively small roughness. Since there is no generally accepted bistatic cross section model that deals with both coherent and incoherent reflections of sea surfaces, the model in [42] is still used in this research. In order to achieve a more

precise surface description in the future, a term which would account for the coherent reflections from relatively flat areas should be considered. Similar analysis to the land surface remote sensing of SAR reflections in [68] may be undertaken.

Generally, oil slick detection using GNSS-R holds a promising future. It could be used to complement the result of existing space-based oil slick detection method. Further work is required to increase the performance of this technique, especially for the cases with small scale oil spills. It is possible to further increase the accuracy by using better de-noising techniques. As for improving retrieval resolution, increasing the processed SNR using better receiving configurations is one possible solution. Another potential method is to use the GPS L5 signal which has a shorter PRN chip length. The much shorter chip length of the L5 signal is expected to greatly improve the achievable surface resolution and allow surface mapping in more detail.

To better evaluate the performance of 2-D LS fitting for wind retrieval, the actual antenna pattern from calibrated data must be employed. Also, further improvements to this approach could be achieved if the bias of the receiver clock can be estimated. It is expected that the work presented will prove fruitful in augmenting the role of GNSS-R as an ocean surface sensor.

Bibliography

[1] F.T. Ulaby, R.K. Moore and A.K. Fung, *Microwave remote sensing: Active and passive; volume II: Radar remote sensing and surface scattering and emission theory*, Artech House 1982.

[2] I. S. Robinson, *Satellite oceanography: An introduction for oceanographers and remote-sensing scientists*, Wiley, 1994.

[3] A. Komjathy, V. U. Zavorotny, P. Axelrad, G. H. Born, and J. L. Garrison, "GPS signal scattering from sea surface: Wind speed retrieval using experimental data and theoretical model," *Remote Sens. Environ.*, vol. 73, no. 2, pp. 162-174, 2000.

[4] T. Elfouhaily, B. Chapron, K. Katsaros, and D. Vandemark, "A unified directional spectrum for long and short wind-driven waves," *J. Geophys. Res.*, vol. 102, no. C7, pp. 15781-15796, 1997.

[5] S. Gleason, S. Hodgart, Y. Sun, C. Gommenginger, S. Mackin, M. Adjrad, and M. Unwin, "Detection and processing of bistatically reflected GPS signals from low Earth orbit for the purpose of ocean remote sensing," *IEEE Trans. Geosci. Remote Sens.*, vol. 43, no. 6, pp. 1229-1241, Jun. 2005.

[6] M. Belmonte, P. Axelrad and D. Masters., "GPS reflections from sea ice," Presented at the GNSS Reflections Workshop 2005, University of Surrey, 2005.

[7] S. Gleason, "Towards sea ice remote sensing with space detected GPS signals: demonstration of technical feasibility and initial consistency check using low resolution sea ice information," *Remote Sens.* vol. 2, pp. 2017-2039, 2011.

[8] K.M. Golden, D. Borup, M. Cheney, E. Cherkaeva, M.S. Dawson, K.-H. Ding, A.K. Fung, D. Isaacson, S.A. Johnson, A.K. Jordan, J.A. Kong, R. Kwok, S.V. Nghiem, R.G. Onstott, J. Sylvester, D.P. Winebrenner, I.H.H. Zabel, "Inverse electromagnetic scattering models for sea ice," *IEEE Trans. Geosci. Remote Sens.* vol. 36, no. 5, pp. 1675-1704, 1998.

[9] D.J. Cavalieri, "A Microwave technique for mapping thin sea ice," *J. Geophys. Res.* vol. 99, no. C6, pp. 12562-12572, 1994.

[10] T.C. Grenfell, D.G. Barber, A.K. Fung, A.J. Gow, K.C. Jezek, E.J. Knapp, S.V. Nghiem, R.G. Onstott, D.K. Perovich, C.S. Roesler, C.T. Swift, F. Tanis, "Evolution of electromagnetic signatures of sea ice from initial formation to the establishment of thick first-year ice," *IEEE Trans. Geosci. Remote Sens.* vol. 36, no. 5, pp. 1642-1654, 1998.

[11] T. Toyota, K. Nakamura, and S. Uto, "Retrieval of ice thickness distribution in the seasonal ice zone from L-band SAR," *Int. J. Remote Sens.* vol. 30, no. 12, pp. 3171-3189, 2009.

[12] M. Wiehl, B. Legresy, R. Dietrich, "Potential of reflected GNSS signals for ice sheet remote sensing," *Prog. Electromagn. Res.* vol. 40, pp. 177-205, 2003.

[13] S.J. Katzberg, O. Torres, M.S Grant and D. Masters. "Utilizing calibrated GPS reflected signals to estimate soil reflectivity and dielectric constant: Results from SMEX," *Remote Sens. Environ.* vol. 100, no. 1, pp. 17-28, 2005.

[14] J. F. Marchan-Hernandez, N. Rodriguez-Alvarez, A. Camps, X. Bosch-Lluis, I. Ramos-Perez, and E. Valencia, "Correction of the sea state impact in the L-band brightness temperature by means of Delay-Doppler Maps of Global Navigation Satellite Signals reflected over the sea surface," *IEEE Trans. Geosci. Remote Sens.* vol. 46, no. 10, pp. 2914-2923, 2008.

[15] O. Germain, "The eddy experiment: GNSS-R speculometry for directional sea-roughness retrieval from low altitude aircraft," *Geophys. Res. Lett.* vol. 31, no. 21, 2004.

[16] M. Clarizia, C. Gommenginger, S. Gleason, M. Srokosz, C. Galdi, and M. Bisceglie, Analysis of GNSS-R delay-Doppler maps from the UK-DMC satellite over the ocean, *Geophys. Res. Lett.*, vol. 36, no. 2, 2009.

[17] S. Gleason, "Remote sensing of ocean, ice and land surfaces using bistatically scattered GNSS signals from low earth orbit," PhD Thesis, University of Surrey, 2006.

[18] P. Beckmann and A. Spizzichino, "The scattering of electromagnetic waves from rough surfaces," Artech House 1987.

[19] D. E. Barrick, "Rough surface scattering based on the specular point theory," *IEEE Trans. Antennas Propag.,* vol. 16, no. 4, pp. 449-454, 1968.

[20] A. Stoffelen and D. Anderson, "Ambiguity removal and assimilation of scatterometer data," *Quart. J. Roy. Meteor. Soc.,* vol. 123, no. 538, pp. 491-518, 1997.

[21] E. Andersson, J. Haseler, P. Unden, P. Courtier, G. Kelly, D. Vasiljevic, C. Brankovic, C. Gaffard, A. Hollingsworth, C. Jakob, "The ECMWF implementation of three-dimensional variational assimilation (3D-Var). III: Experimental results," *Quart. J. Roy. Meteor. Soc.,* vol. 124, no. 550, pp. 1831-1860, 1998.

[22] A. Bentamy, Y. Quilfen and P. Flament, "Scatterometer wind fields - a new release over the decade 1991-2001," *Can. Jour. of Rem. Sens.,* vol. 28, no. 3, 2002.

[23] N. Grima, A. Bentamy, K. Katsaros, Y. Quilfen, P. Delecluse, C. Levy, "Sensitivity of an oceanic general circulation model forced by satellite wind stress fields," *J. Geophys. Res.,* vol. 104, C4, pp. 7967-7989, 1999.

[24] Y. Quilfen, A. Bentamy, P. Delecluse, K. Katsaros, N. Grima, "Prediction of sea level anomalies using ocean circulation model forced by scatterometer wind and validation using TOPEX/Poseidon data," *IEEE Trans. Geosci. Remote Sens.,* vol. 38, no. 4, pp. 1871-1884, 2000.

[25] A. Stoffelen, "Scatterometry," Phd thesis at the University of Utrecht, 1998.

[26] "abs NEWS." Internet: `http://abcnews.go.com/US/exclusive-submarine-dive-finds-oil-dead-sea-life/story?id=12305709`

[27] S. T. Lowe, J. L. LaBrecque, C. Zuffada, L. J. Romans, L. E. Young and G. A. Hajj, "First spaceborne observation of an Earth-reflected GPS signal," *Ratio Sci.*, vol. 37, no. 1, pp. 7-1-7-28, 2002.

[28] S. Gleason, C. Gommenginger, and D. Cromwell, "Fading statistics and sensing accuracy of ocean scattered GNSS and altimetry signals," *J. Adv. Space Res.*, vol. 46, no. 2, pp. 208–220, 2009.

[29] D. R. Thompson, T. M. Elfouhaily, and J. L. Garrison, "An improved geometrical optics model for bistatic GPS scattering from the ocean surface," *IEEE Trans. Geosci. Remote Sens.*, vol. 43, no. 12, pp. 2810–2821, 2005.

[30] S. Jin, G.P. Feng, and S. Gleason, "Remote sensing using GNSS signals: Current status and future directions," *Adv. Space Res.*, vol. 47, no. 10, pp. 1645-1653, 2011.

[31] M. Martin-Neira, "A passive reflectometry and interferometry system (PARIS): Application to ocean altimetry," *ESA J.*, vol. 17, pp. 331–355, 1993.

[32] J. L. Garrison, S. J. Katzberg, M. I. Hill, "Effect of sea roughness on bistatically scattered range coded signals from the Global Positioning System," *Remote Sens.* vol. 25, pp. 2257-2260, 1998.

[33] J. L. Garrison, A. Komjathy, V. Zavorotny and S. J. Katzberg, "Wind speed measurement using forward scattered GPS signals," *IEEE Trans. Geosci. Remote Sens.*, vol. 40, no. 1, pp. 50-65, 2002.

[34] E. Valencia, "Ocean surface's scattering coefficient retrieval by delay-Doppler map inversion," *IEEE Geosci. Remote Sens. Lett.*, vol. 8, no. 4, pp. 750-754, 2011.

[35] N. Rodriguez-Alvarez, D.M. Akos, V.U. Zavorotny, J.A. Smith, A. Camps and C.W. Fairall. , "Airborne GNSS-R wind retrievals using Delay-Doppler maps," *IEEE Trans. Geosci. Remote Sens.*, vol. 51, no. 1, 2013.

[36] E. Valencia, A. Camps, H. Park, and N. Rodriguez-Alvarez, "Oil slicks detection using GNSS-R," in *Proc. IGARSS*, pp. 4383 - 4386, 2011.

[37] E. Valencia, A. Camps, N. Rodriguez-Alvarez, H. Park, and I. Ramos-Perez, "Using GNSS-R Imaging of the Ocean Surface for Oil Slick Detection," *IEEE J. Sel. Topics Appl. Earth Observ.*, vol. 6, no. 1, pp. 217-223, 2013.

[38] M. Martin-Neira, S. D' Addio, C. Buck, N. Floury, and R. Pietro-Cerdeira, "The PARIS ocean altimeter in-orbit demonstrator," *IEEE Trans. Geosci. Remote Sens.* vol.49, no.6, pp. 2209-2237, June 2011.

[39] J.F. Marchan-Hernandez, A. Camps, N. Rodriguez-Alvarez, E. Valencia, X. Bosch-Lluis, and I. Ramos-Perez, "An efficient algorithm to the simulation of delay-Doppler maps of reflected globa navigation satellite system signals," *IEEE Trans. Geosci. Remote Sens.* vol. 47, no. 8, pp. 2733-2740, 2009.

[40] H. Park, E. Valencia, and N. Rodriguez-Alvarez, "A new approach to sea surface wind retrieval from GNSS-R measurements," in *Proc. IEEE IGARSS*, pp. 1469-1472, 2011.

[41] C. Li and W. Huang, "Sea surface oil slick detection from GNSS-R Delay-Doppler Maps using the Spatial Integration Approach," *IEEE Radar Conf.*, Ottawa, Canada, 2013.

[42] V.U. Zavorotny and A.G. Voronovich, "Scattering of GPS signals from the ocean with wind remote sensing application," *IEEE Trans. Geosci. Remote Sens.* vol. 38, no. 2, pp. 951-964, 2000.

[43] "Wikipedia, Geodetic system." Internet: `http://en.wikipedia.org/wiki/Geodetic_system`

[44] S. Gleason, V. Zavorotny and S. Lowe, "Remote sensing using bistatic GNSS reflections," in *GNSS Applications and Methods*, S. Gleason and D. Gebre-Egziabher (editors), Artech House, 2009.

[45] A. R. Hayslip, J. T. Johnson, G. R. Baker, "Further numerical studies of backscattering from time-evolving nonlinear sea surfaces," *IEEE Trans. Geosci. Remote Sens.*, vol. 41, no. 10, 2287-2293, 2003.

[46] G. Franceschetti, A. Iodice, D. Riccio, G. Ruello, R. Siviero, "SAR raw signal simulation of oil slicks in ocean environments," *IEEE Trans. Geosci. Remote Sens.*, vol. 40, no. 9, pp. 1935-1949, 2002.

[47] C. Li and W. Huang, "Simulating GNSS-R Delay-Doppler map of oil slicked sea surface under general," *Prog. Electromagn. Res. B*, vol. 48, pp. 61-76, 2013.

[48] C. Li and W. Huang, "A simulation process of delay-Doppler maps of oil slicked sea surfaces under general scenarios," in *Proc. IEEE NECEC*, Newfoundland, Canada, 2012.

[49] C. Cox and W. Munk, "Measurements of the roughness of the sea surface from photographs of the suns glitter," *J. Opt. Soc. Am.*, vol. 44, no. 11, pp. 838–850, 1954.

[50] S. J. Katzberg, O. Torres, and G. Ganoe, "Calibration of reflected GPS for tropical storm wind speed retrievals," *Geophys. Res. Lett.*, vol. 33, no. 18, 2006.

[51] "NASA, MODIS imagery." Internet: `http://modis.gsfc.nasa.gov/gallery/`

[52] "National Data Buoy Center." Internet: `http://www.ndbc.noaa.gov/station_history.php?station=42040`

[53] H. Masuko, K. Tatsuharu and O. Kenichi, "Observation of artificial slicks with SIR-C/X-SAR around Japan," in *Proc. IEEE IGARSS*, pp. 227-229, July 1995.

[54] C. Ruf, S. Gleason, Z. Jelenak, S. Katzberg, A. Ridley, R. Rose, J. Scherrer and V. Zavorotny, "The CYGNSS nanosatellite constellation hurricane mission," in *Proc. IEEE IGARSS*, Munich, German, 2012.

[55] M. Gade, W. Alpers and M. Bao, "Measurements of the radar backscattering over different oceanic surface films during the SIR-C/X-SAR campaigns," in *Proc. IEEE IGARSS*, 1996.

[56] R. C. Gonzales and R. E. Woods, *Digital Image Processing*. Upper Saddle River, NJ: Prentice Hall, 2002.

[57] S. Gleason, "Space-based GNSS scatterometry: Ocean wind sensing using an empirically calibrated model," *IEEE Trans. Geosci. Remote Sens.*, vol. 51, no. 9, pp. 4853 - 4863, 2013.

[58] A. Moccia and A. Renga, "Spatial resolution of bistatic synthetic aperture radar: impact of acquisition geometry on imaging performance," *IEEE Trans. Geosci. Remote Sens.*, vol. 49, no. 10, pp. 3487-3503, 2011.

[59] P. Sebastiao, C. Guedes Soares, "Modeling the fate of oil spills at sea," *Spill Sci. Technol. B.*, vol. 2, no. 2, pp. 121–131, 1995.

[60] T. Azwell, M. J. Blum, A. Hare, S. Joye, S. Kubendran, A. Laleian, G. Lane, D. J. Meffert, E.B. Overton, J. Thomas, "The Macondo blowout environmental report," *Deepwater Horizon Study Group Environmental Report*, 2011.

[61] European Space Agency, "Oil pollution monitoring," *ESA Brochure: ERS and Its Applications–Marine*, vol. 1, BR–128, 1999.

[62] C. Li and W. Huang, "Land scattering coefficient distribution retrieval from GNSS-R signals," in *Proc. IEEE NECEC*, Newfoundland, Canada, 2013.

[63] C. Cox and W. Munk, "Measurement of the roughness of the sea surface from photographs of the sun's glitter,"*J. Opt. Soc. Am.*, vol. 44, no. 11, pp. 838-850, Nov 1954.

[64] C. Li and W. Huang, "Sea surface wind retrieval from GNSS delay-Doppler map using two-dimension least-squares fitting," in *Proc. IEEE OCEANS*, Bergen, Norway, 2013.

[65] W. Huang and E. Gill, "Surface current measurement under low sea state using dual polarized X-band nautical radar," *IEEE J. Sel. Topics Appl. Earth Observ. Remote Sens.*, vol. 5 no. 6, pp. 1868-1873, 2012.

[66] S. A. Hsu, E. A. Meindl, and D. B. Gilhousen, "Determining the power-law wind-profile exponent under near-neutral stability conditions at sea," *J. Appl. Meteorol.*, vol. 33, no. 6, pp. 757–765, 1994.

[67] E. Valencia, V. U. Zavorotny, D. M. Akos, and A. Camps, "Using DDM asymmetry metrics for wind direction retrieval from GPS ocean-scattered signals in airborne experiments," *IEEE Trans. Geosci. Remote Sens.*, vol. 52, no. 7, pp. 3924-3936, 2014.

[68] N. Pierdicca, L. Pulvirenti, F. Ticconi, and M. Brogioni, "Radar bistatic configurations for soil moisture retrieval: a simulation study," *IEEE Trans. Geosci. Remote Sens.*, vol. 46, no. 10, pp. 3252-3264, 2008.